

1 **First-principles theory for Earth's tropical-midlatitude climate boundary**

2 Tsubasa Kohyama*, Hiroaki Miura, and Kazuya Yamazaki

3 *Department of Information Sciences, Ochanomizu University, Tokyo, Japan*

4 *Department of Earth and Planetary Science, The University of Tokyo, Tokyo, Japan*

5 *Information Technology Center, The University of Tokyo, Chiba, Japan*

**This is a non-peer-reviewed preprint
submitted to EarthArXiv.**

6 *Corresponding author address: Department of Information Sciences, Ochanomizu University,

7 2-1-1, Bunkyo-ku, Tokyo, Japan, 112-8610

8 E-mail: tsubasa@is.ocha.ac.jp

ABSTRACT

9 In Earth’s climate, the boundary between the tropics and midlatitudes
10 is a key determinant of temperature and precipitation characteristics¹,
11 influencing human societies through daily weather^{2,3}, atmospheric chem-
12 istry⁴, carbon cycling⁵, and vegetation distribution^{6,7}. The physical ori-
13 gin of these climate zones has been investigated through idealized sim-
14 ulations⁸⁻¹⁴, observations^{15,16}, and state-of-the-art climate models¹⁷⁻²⁰.
15 However, a first-principles theory to explain the boundary position re-
16 mains largely unexplored. Here we propose a theory to understand this
17 climate bifurcation based on the first law of thermodynamics. We intro-
18 duce a dimensionless parameter, the thermal-mechanical ratio (\mathcal{T}/\mathcal{M}),
19 to quantify the roles of thermal and mechanical sources for driving verti-
20 cal motion. This parameter offers a first-principles definition of “trop-
21 icalness”: regions where thermal contribution dominates are tropical
22 ($\mathcal{T}/\mathcal{M} \gtrsim 10$), whereas regions with non-negligible mechanical contri-
23 butions are midlatitudinal ($\mathcal{T}/\mathcal{M} \lesssim 10$). We derive a simple model to
24 describe the determination mechanism of the boundary position from
25 fundamental physical constants, which explains observed annual clima-
26 tology, seasonal variability, global warming response, and the El Niño-
27 Southern Oscillation sensitivity. This framework provides robust the-
28 oretical foundations for understanding anthropogenic tropical expan-
29 sion^{21,22}, informing climate change adaptation strategies²³. Applications
30 to other planetary atmospheres are also suggested^{24,25}.

31 **Introduction**

32 Earth contains distinct tropical and midlatitude climate zones. The tropics maintain warm, hu-
33 mid conditions throughout the year with vigorous convective rainfall as the dominant precipitation
34 mechanism. By contrast, the midlatitudes exhibit pronounced seasonality, with frontal cyclones
35 as the primary precipitation source. The boundary between the tropics and the midlatitudes de-
36 termines a wide range of climate elements, such as temperature distribution^{1,3}, the genesis and
37 decay regions of tropical cyclones²⁶, precipitation patterns^{2,27}, and atmospheric chemistry⁴. This
38 climate boundary governs the climate of regions where approximately half the global population
39 resides²², in addition to defining vegetation and ecosystem^{28,29}, exerting diverse influences on the
40 entire Earth's system.

41 The fundamental difference between these two climate zones stems from the latitude-dependent
42 relative importance of solar heating and Earth's rotation. In the tropics, heating dominates over ro-
43 tational effects, so vertical convective motion driven by local heating plays a paramount role. In the
44 midlatitudes, rotation dominates, making the relaxation of meridional temperature gradients the
45 primary driving source. Similar physical mechanisms also appear in other planetary atmospheres
46 such as the Martian atmosphere^{24,25}, indicating universal features of planetary atmospheres.

47 Research over the past decades includes idealized simulations⁸⁻¹⁴, phenomenological descrip-
48 tions^{15,16}, and global climate model experiments¹⁷⁻²⁰ to understand the tropical-midlatitude (T/M)
49 boundary latitude, yielding valuable theoretical insights. Despite these excellent contributions,
50 however, incorporating complex atmospheric behaviors (e.g., atmospheric stability, moist pro-
51 cesses, and eddy effects) into first-principles explanations remains difficult. Currently, quantita-
52 tive predictions of boundary fluctuations and future changes rely on phenomenon-specific physical
53 arguments that depend heavily on observational data and/or model assumptions.

54 As an implication for social impacts, a poleward shift of the T/M boundary, which is referred
55 to as the “tropical expansion”, is believed to cause discontinuous climate changes across wide
56 regions on Earth^{15,21}. This expansion threatens local agriculture and water resources, which makes
57 societal infrastructure reconstruction inevitable in the near future²³. However, numerous studies
58 employ a large variety of phenomenological bases to project the expansion, leaving no consensus
59 on quantitative estimates such as warming-induced expansion rates²².

60 These circumstances demand a unified understanding of the T/M boundary behavior based on
61 first principles. Hence, this study proposes a theory to understand what bifurcates the tropics and
62 the midlatitudes. Based on physically robust minimal assumptions, this framework explains the
63 boundary position climatology, seasonal variability, global warming responses, and interannual
64 variations. Our theory deepens understanding of Earth’s climate, as well as providing new per-
65 spectives for adjacent fields including ecosystem distributions and other planetary atmospheres.

66 **The T/M theory**

67 The first law of thermodynamics for a unit mass of air reads:

$$-\alpha\omega = j - c_p \frac{DT}{Dt} \quad (1)$$

68 where α is specific volume (inverse density), ω is pressure change rate (equivalent to vertical
69 motion under hydrostatic balance, with $\omega < 0$ for upward motion), j is diabatic heating rate, c_p is
70 specific heat at constant pressure, and DT/Dt is temperature tendency. Under hydrostatic balance,
71 the equation (1) can be interpreted as a decomposition of vertical motion into thermally- and
72 mechanically-determined components. Therefore, we hereafter call the first term of the right-hand
73 side the “thermal source” and the second term the “mechanical source”.

74 These two sources are physically distinct. The thermal source j drives vertical motion by acting
75 on the thermodynamic state within the air parcel through molecular-scale processes, such as radia-
76 tion and surface heat flux, without necessarily requiring air temperature changes. By contrast, the
77 mechanical source $-c_p DT/Dt$ constrains vertical motion through adiabatic adjustment to large-
78 scale dynamic conditions outside the air parcel, manifesting as an air temperature change as a
79 macroscopic property of the molecular ensemble. Critically, atmospheric circulation structure and
80 response characteristics differ fundamentally depending on which source balances vertical motion
81 (*see* Supplementary Text 1 for details).

82 Here we propose to define the tropics as regions where the thermal source dominates over the
83 mechanical source, and the midlatitudes as regions where the mechanical source remains signif-
84 icant. Therefore, we introduce a dimensionless parameter to characterize the relative importance
85 of these two sources, the thermal-mechanical ratio (T/M ratio):

$$\mathcal{T}/\mathcal{M} := \left| \frac{[j]}{[-c_p DT/Dt]} \right| \simeq \left| \frac{[j]}{gDZ_T/Dt} \right| \sim \frac{J}{fU^2} \cdot \frac{L^2}{L_R^2} \quad (2)$$

86 where $[\]$ denotes mass-weighted vertical average over the troposphere, g is gravitational accelera-
87 tion, Z_T is tropopause height, J is the scale of diabatic heating per unit mass, f is the magnitude of
88 the Coriolis parameter, U is typical wind speed scale, L is typical horizontal scale, and L_R is the
89 Rossby deformation radius. Setting the criterion for negligibility at one-tenth, regions with \mathcal{T}/\mathcal{M}
90 $\gtrsim 10$ follow tropical dynamics, whereas regions with $\mathcal{T}/\mathcal{M} \lesssim 10$ follow midlatitude dynamics.

91 The symbols \simeq and \sim in equation (2) hold under hydrostatic balance and quasi-geostrophic
92 balance assumptions, respectively (*see* Methods), making $\mathcal{T}/\mathcal{M} \sim J/(fU^2 L_R^2/L^2)$ a widely ap-
93 plicable scaling for large-scale atmospheric motion. The thermal source $\mathcal{T} \sim J$ matches the rate
94 of energy conversion from diabatic heating to kinetic energy, primarily determined by the differ-
95 ence between incoming solar and outgoing thermal radiation (though incoming radiation may first

96 warm the surface before injection as sensible or latent heat; J includes all net diabatic heating).
 97 Conversely, the mechanical source $\mathcal{M} \sim fU^2L_R^2/L^2$ matches the rate of conversion from available
 98 potential energy to kinetic energy (baroclinic energy conversion), determined primarily by Earth's
 99 rotation rate and atmospheric flow state.

100 As the simplest treatment of the T/M ratio, we could consider its large and small limits.
 101 The former represents thermally-dominated tropical dynamics, whereas the latter represents
 102 mechanically-dominated midlatitude dynamics. Indeed, taking $\mathcal{T}/\mathcal{M} \rightarrow \infty$ in the atmospheric ba-
 103 sic equations yields the well-known governing equations for the tropics (Weak Temperature Gradi-
 104 ent (WTG) system)³⁰, whereas taking $\mathcal{T}/\mathcal{M} \rightarrow 0$ yields those of midlatitudes (Quasi-geostrophic
 105 potential vorticity conservation system)³¹ (Supplementary Text 2).

106 To discuss the transition zone between the tropical and midlatitude extremes, we must choose the
 107 horizontal scale appropriately for coarse-graining. When horizontal scales are too small, convec-
 108 tion and individual disturbances are not spatially averaged, so we cannot consider the large-scale
 109 dynamical structure that defines the boundary. Conversely, when horizontal scales are too large,
 110 spatial averaging through coarse-graining encompasses both tropical and midlatitude character-
 111 istics, losing the ability to resolve the climate regime bifurcation. Therefore, to balance these
 112 considerations, we choose a typical horizontal scale of large-scale fields to satisfy $L^2 \sim 10L_R^2$.

113 The ‘‘T/M boundary layer’’, where $\mathcal{T}/\mathcal{M} \sim 10$, smoothly connects the two interior regions
 114 governed by different atmospheric dynamics. The condition for the T/M boundary layer obtained
 115 from the above coarse-graining, considering the scaling in equation (2), simplifies to:

$$\mathcal{T} \sim 10\mathcal{M} \text{ AND } L^2 \sim 10L_R^2 \implies J \sim fU^2 \quad (3)$$

116 This relation becomes crucial when constructing the conceptual model in the next section.

117 Under the above coarse-graining, \mathcal{T}/\mathcal{M} varies over Earth with orders ranging from 10^{-1} to
 118 10^3 . Therefore, when analyzing spatiotemporal variations of \mathcal{T}/\mathcal{M} , it is convenient to examine
 119 climatology, deviations, and trends of $\log_{10}(\mathcal{T}/\mathcal{M})$. For climatological means (denoted by over-
 120 line), the approximation $\overline{\log_{10}(\mathcal{T}/\mathcal{M})} \simeq \log_{10}(\overline{\mathcal{T}/\mathcal{M}})$ generally holds with good precision, but
 121 we must note that $\overline{\log_{10}(\mathcal{T}/\mathcal{M})} \neq \log_{10}(\overline{\mathcal{T}/\mathcal{M}})$.

122 **Theoretical prediction and observational validation of the T/M boundary latitude**

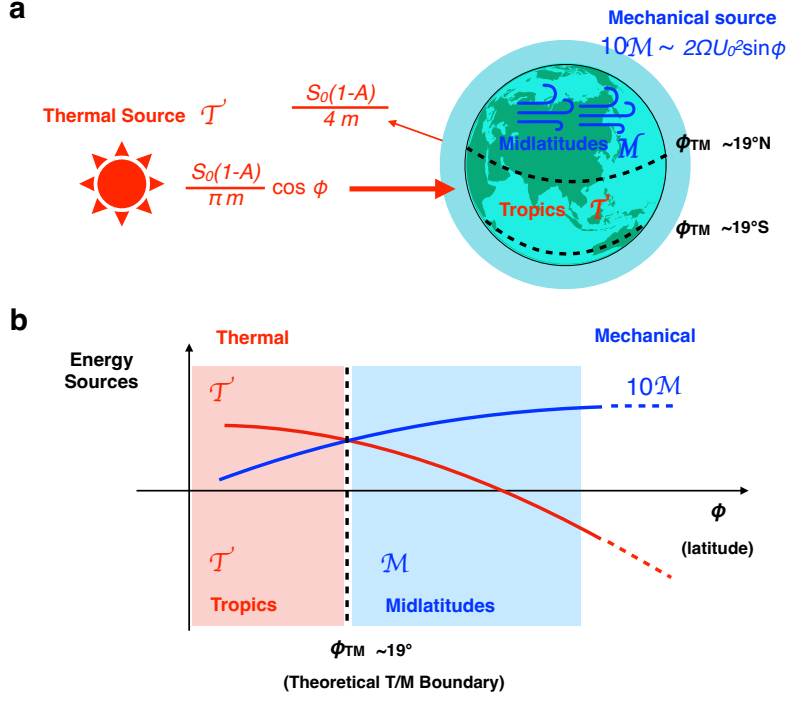
123 *Annual climatology of the T/M boundary*

124 The T/M boundary is where the orders of thermal and mechanical sources intersect. To under-
 125 stand the determination mechanism of the T/M boundary latitude from first principles, we consider
 126 the static model shown in Fig. 1. Mathematical and physical details appear in Methods, summa-
 127 rized below.

132 First, the scale $\mathcal{T} \sim J$ of the thermal source becomes a monotonically decreasing function of lat-
 133 itude ϕ , due to the local energy imbalance between incoming solar radiation and outgoing thermal
 134 radiation. Here, we represent outgoing radiation by its global-mean value, assuming that atmo-
 135 spheric and oceanic circulation adjust this energy imbalance faster than the climatic timescale.
 136 Conversely, the scale of the mechanical source $10\mathcal{M} \sim fU^2$ becomes a monotonically increasing
 137 function of ϕ in the latitude bands of interest, since Coriolis force increases from equator to pole
 138 with the sine of latitude.

139 Based on equation (3), the T/M boundary latitude ϕ_{TM} is obtained as the solution to $J(\phi) =$
 140 $f(\phi)U(\phi)^2$, namely:

$$\frac{S_0(1-A)}{\pi m} \cos \phi - \frac{S_0(1-A)}{4m} = (2\Omega \sin \phi)(U(\phi))^2 \quad (4)$$



128 FIG. 1. **Theoretical framework of the Thermal-Mechanical (T/M) theory showing the relationship be-**
 129 **tween enthalpy sources and climate regimes.** **a**, Conceptual model considered in this study. **b**, The diagram
 130 illustrates how the ratio of thermal (\mathcal{T}) to mechanical (\mathcal{M}) energy sources determines the boundary between
 131 tropical and midlatitude dynamics.

141 where S_0 is the solar constant, A is Earth's albedo, π is the mathematical constant, m is the
 142 vertically-integrated atmospheric mass per unit area, and Ω is Earth's angular velocity. As a
 143 zeroth-order approximation, we treat A and m as global constants. In this study, we hereafter
 144 use $S_0 = 1,366 \text{ W/m}^2$, $A = 0.3$, $m = 10,327 \text{ kg/m}^2$, and $\Omega = 7.27 \times 10^{-5} \text{ /s}$.

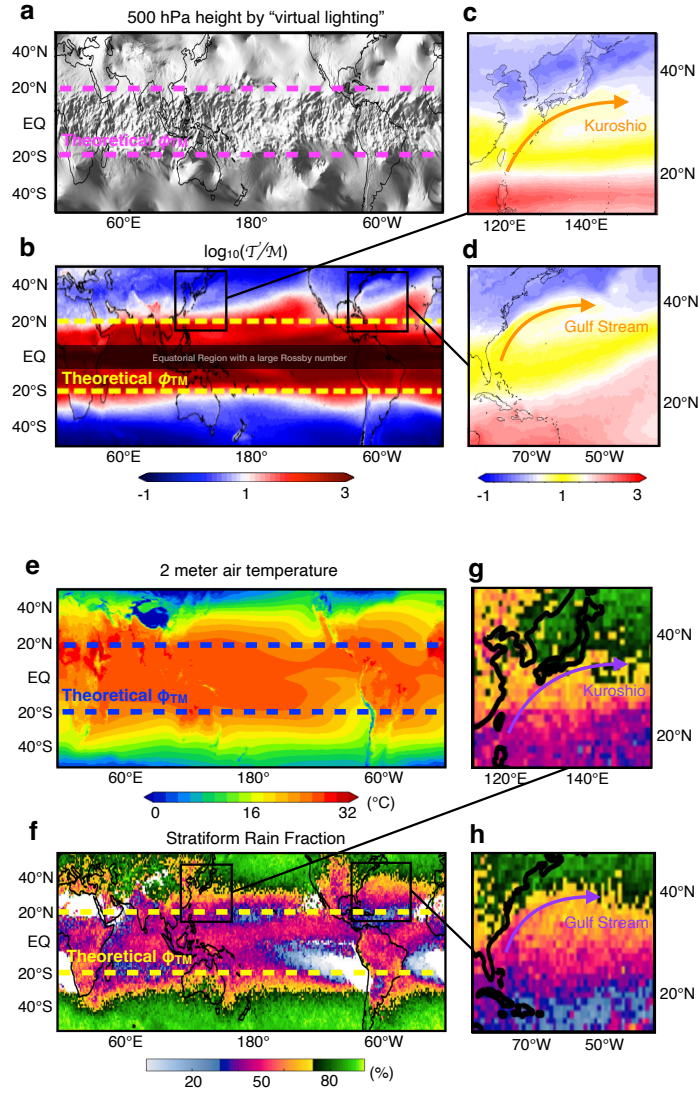
145 Now, by defining $U_0 := U(\phi_{TM})$ as the input parameter representing the typical wind speed at
 146 the T/M boundary, the first-principles model given by equation (4) yields an analytical solution:

$$\phi = \phi_{TM}(U_0) := \arctan\left(\frac{S_0(1-A)}{2\Omega U_0^2 \pi m}\right) - \arcsin\left(\frac{S_0(1-A)}{4m\sqrt{4\Omega^2 U_0^4 + S_0^2(1-A)^2/\pi^2 m^2}}\right) \quad (5)$$

147 For example, by adopting $U_0 = 10$ m/s as a representative tropospheric wind-scale parameter, the
148 model yields $\phi_{\text{TM}} \simeq 19.0^\circ$, which serves as a first-order estimate of the T/M boundary latitude as
149 validated below.

158 Atmospheric behavior fundamentally differs between the tropical and midlatitudinal sides of
159 the T/M boundary. The above theoretical value can be validated in detail using reanalysis data,
160 which is obtained by assimilating observations into weather prediction models. Figures 2a and
161 2b show the 500 hPa geopotential height visualized using “virtual lighting” (*see* Methods), and
162 annual climatology of $\log_{10}(\mathcal{T}/\mathcal{M})$, respectively. The 500 hPa height field suggests that small-
163 scale disturbances dominate in the tropics, whereas large-scale pressure gradients dominate in the
164 midlatitudes. This contrast is overall consistent with the $\log_{10}(\mathcal{T}/\mathcal{M})$ distribution, which shows
165 that local heating (large-scale pressure adjustment) balances vertical motion in the tropics (midlat-
166 itudes). The zonal-mean T/M boundary latitude calculated from the reanalysis \mathcal{T}/\mathcal{M} distribution
167 (1982-2024 average) is located around 27° . The $\sim 8^\circ$ difference between the simple model and
168 observations is a reasonable discrepancy, attributable to the simplicity of the zeroth-order model,
169 including the choice of the model input $U_0 = 10$ m/s and the neglect of approximately one-tenth of
170 meridional heat transport by both oceanic and atmospheric dynamics.

171 The T/M boundary is a crucial demarcation that characterizes Earth’s climate system. Figure
172 2e shows annual-mean 2-meter air temperature. Only equatorward of the T/M boundary, spatial
173 temperature variations are small (i.e., isotherms are nearly absent). Figure 2f shows stratiform
174 rainfall fraction derived by Schumacher and Funk (2023)²⁷, with the T/M boundary positioned
175 near the 50% contours. Convective rainfall dominates tropical regions, whereas stratiform rainfall
176 increases sharply toward the midlatitudes. This contrast confirms the T/M theory’s implications,
177 i.e., the tropics are dominated by vertical mixing with local, thermally-driven convection (e.g.,
178 cumulonimbus), whereas the midlatitudes are dominated by the large-scale systems to relax the

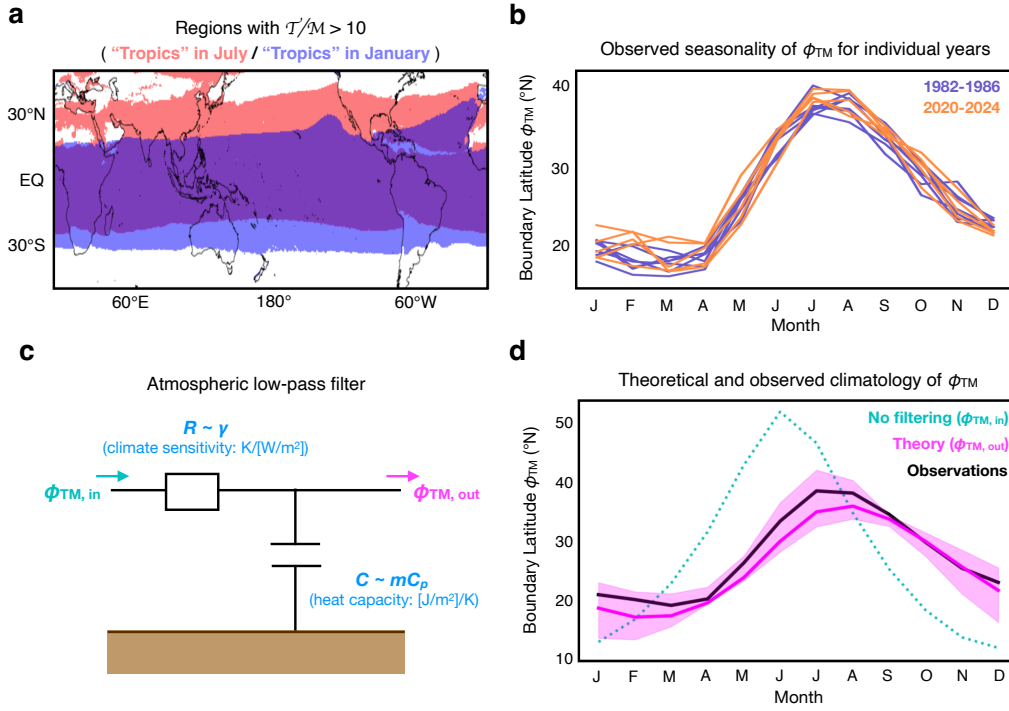


150 **FIG. 2. Observational validation of the T/M theory and its implications for air temperatures and rain-**
 151 **fall.** (a) 500 hPa geopotential height visualization using “virtual lighting” (3:00 Universal Time Coordinated
 152 (UTC) on April 20, 2024). (b) Annual climatology of $\log_{10}(\mathcal{T}/\mathcal{M})$. The equatorial region is masked because
 153 the scaling in Eqn. (2) is not valid. (c,d) As in (b), but for the Kuroshio and the Gulf Stream regions indicated by
 154 the black boxes in (b). (e) Annual climatology of 2-meter air temperature. (f) Annual climatology of stratiform
 155 rain fraction by Schumacher and Funk (2023)²⁷. (g, h) As in (f), but for the Kuroshio and the Gulf Stream
 156 regions. The dashed lines in (a), (b), (e), and (f) represent the theoretical T/M boundary of $\phi_{TM} = \pm 19.0^\circ$. Also
 157 shown as solid arrows in (c), (d), (g), and (h) are the approximate positions of the major ocean warm currents.

179 global, meridional density gradients (e.g., extratropical cyclones). In addition, pressure, humidity,
180 potential vorticity, and convective indices exhibit similar contrasts between climate zones (Sup-
181 plementary Fig. 3).

182 At the T/M boundary, mechanical source contribution gradually increases toward the poles, cre-
183 ating a “phase transition” from tropical to midlatitude dynamics. Indeed, the “T/M boundary
184 layer” forms near $T/M \sim 10$ (Fig. 2b, white), where singular behavior emerges due to the coexis-
185 tence of both tropical and midlatitude characteristics. Furthermore, at the continental east coasts,
186 strong heating from oceanic warm currents lets the T/M boundary layer intrude into the midlat-
187 itudes (“tropical spillover”). Figures 2c and 2d show $\log_{10}(\mathcal{T}/\mathcal{M})$ distribution in the Kuroshio
188 and Gulf Stream regions, respectively (“T/M boundary layer” highlighted yellow), and Fig. 2g
189 and 2h show stratiform rainfall fraction in these regions. Ocean dynamics not considered in our
190 simple model creates strong warm currents, which serve as local heat sources, locally deforming
191 the T/M boundary. In this spillover region, convective rainfall fraction is higher than surroundings,
192 extending tropical precipitation characteristics into the midlatitudes. This result evidences that the
193 T/M theory has implications even for regional-scale phenomena.

194 As a caveat, though limited in extent, there exist some regions where the T/M ratio estimated by
195 reanalysis appears tropical but the dynamics remain midlatitudinal. For example, at eastern ocean
196 basin coasts such as offshore California, the estimated \mathcal{T}/\mathcal{M} is high (Fig. 2b), yet midlatitude
197 disturbances remain active in the geopotential height and potential vorticity fields (Fig. 2a and
198 Supplementary Fig. 3c). One plausible cause of this discrepancy may be the neglect of zonal
199 variations in the Rossby deformation radius L_R in the T/M ratio estimation by scaling, rather than
200 a failure of the theory itself. For example, if the Rossby deformation radius L_R is larger than the
201 zonal mean, as is the case in the stable eastern basin, the coarse-graining scale $L \sim \sqrt{10}L_R$ chosen
202 in our study leads to an overestimation of the T/M ratio.



204 **FIG. 3. Seasonal migration of the T/M boundary.** (a) Regions with $\mathcal{T}/\mathcal{M} > 10$ during January (blue) and
 205 July (red). (b) Observed seasonality of zonal-mean ϕ_{TM} in the Northern Hemisphere during the first (purple,
 206 1982-1986) and last (orange, 2020-2024) five years of the analysis period. (c) Schematic of the atmospheric
 207 low-pass filter explaining phase lag and amplitude damping in boundary migration. (d) Theoretical prediction
 208 (magenta) and observations (black) of the climatology of zonal-mean ϕ_{TM} in the Northern Hemisphere. In the
 209 former curve, the climate sensitivity of $3\text{ }^\circ\text{C}/(2 \times \text{CO}_2)$ is assumed. The magenta shaded area indicates the
 210 uncertainty of the theoretical prediction estimated by assuming that the climate sensitivity is $1.5\text{-}4.5\text{ }^\circ\text{C}/(2 \times$
 211 $\text{CO}_2)$. Also shown as blue dotted line is the ϕ_{TM} before the atmospheric low-pass filtering.

203 *Seasonal migration of the T/M boundary*

212 The T/M boundary exhibits pronounced seasonal migration. Figure 3a shows the tropical region
 213 ($\mathcal{T}/\mathcal{M} > 10$) in January and July calculated from reanalysis data. The T/M boundary migrates
 214 northward in Northern Hemisphere summer, bringing Tokyo and Los Angeles into the tropics, and
 215 migrates southward in winter, bringing Sydney and São Paulo into the tropics. As shown in Fig.
 216 3b, the zonal-mean Northern Hemisphere T/M boundary remains nearly constant around 20°N

217 from December to April, then abruptly migrates northward from May, reaching its northernmost
 218 extent around 38°N in July before gradually migrating southward. Interestingly, maximum north-
 219 ward migration occurs not in June, when solar radiation is strongest, but one month later in July.
 220 Moreover, as shown later, the peak-to-peak amplitude of observed seasonal variation ($\sim 20^\circ$) is
 221 substantially smaller than the amplitude predicted from solar radiation variation alone ($\sim 40^\circ$).

222 To explain these features, theoretical prediction of seasonal variation proceeds as follows.
 223 First, we introduce seasonal radiation variation effects by replacing $\cos \phi$ in equation (4) with
 224 $h_0 \sin \phi \sin \delta + \cos \phi \cos \delta \sin h_0$ (δ is solar declination, h_0 is hour angle). Next, to account for
 225 transient atmospheric response, we pass the calculated monthly latitudes through an “atmospheric
 226 low-pass filter” that incorporates climate sensitivity and atmospheric heat capacity (*see Methods*).
 227 Specifically, we use the RC low-pass filter circuit equation shown in Figure 3c:

$$\gamma m C_p \frac{d\phi_{\text{TM,out}}(t)}{dt} + \phi_{\text{TM,out}}(t) = \phi_{\text{TM,in}}(t) \quad (6)$$

228 where t is time, γ is climate sensitivity, C_p is specific heat at constant pressure, and $\phi_{\text{TM,in}}$ and
 229 $\phi_{\text{TM,out}}$ are the T/M boundary latitudes before and after filtering, respectively.

230 This theoretical prediction (Figure 3d, magenta line) agrees well with observed seasonal vari-
 231 ation (Figure 3d, black line). Here, observed ϕ_{TM} is obtained as the zonal-mean latitude of the
 232 $\mathcal{T}/\mathcal{M} = 10$ line based on reanalysis data. Following the Intergovernmental Panel on Climate
 233 Change (IPCC) Sixth Assessment Report³², we assume climate sensitivity of 3°C per doubling of
 234 atmospheric CO₂ ($\gamma = 3 \text{ }^\circ\text{C}/(2 \times \text{CO}_2)$). This filtering produces approximately one month phase
 235 lag and reduces amplitude to about 75%. Including climate sensitivity uncertainty of $\gamma = 1.5 - 4.5$
 236 $^\circ\text{C}/(2 \times \text{CO}_2)$, the theoretical curve agrees with observations within the uncertainty range. This
 237 agreement demonstrates that the transient response characteristics of the climate system play es-
 238 sential roles in the T/M boundary variations. It is also notable that the observed T/M boundary

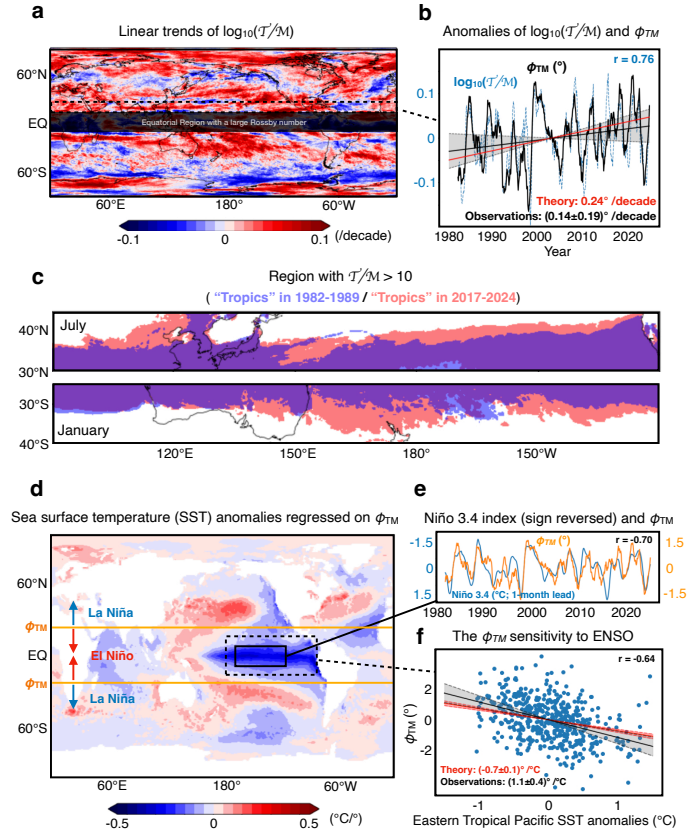
239 variations allow us to estimate the Earth’s climate sensitivity as $1.5\text{-}4.5\text{ }^\circ\text{C}/(2 \times \text{CO}_2)$ in a simple,
240 fundamental manner.

241 Seasonal variability of the T/M boundary latitude exhibits interannual variations and trends.
242 Close inspection of Fig. 3b reveals that interannual variations and tropical expansion trends are
243 particularly large in winter and summer, but are smaller during seasonal transitions in early sum-
244 mer and early autumn. The mechanisms generating such interannual variations and tropical ex-
245 pansion are explored further in subsequent sections.

246 *Tropical expansion caused by global warming*

247 Under global warming, mechanical source contribution decreases over most regions, and ther-
248 mal source contribution becomes relatively more important. Figure 4a shows linear trends of
249 $\log_{10}(\mathcal{T}/\mathcal{M})$ computed at each grid point over the past 40 years. Red regions show increasing
250 T/M ratio (becoming more tropical), whereas blue regions show decreasing T/M ratio (becoming
251 more midlatitudinal). Most regions appear red, particularly from the subtropics to the midlati-
252 tudes, indicating mechanical source contribution decreases and thermal source relative importance
253 increases. We refer to this global tendency as the “global tropicalization”.

267 The T/M boundary latitude has migrated poleward over the past 40 years, and this “tropical
268 expansion” can be understood as a consequence of the aforementioned “global tropicalization.”
269 Figure 4b shows the time series of regional-mean $\log_{10}(\mathcal{T}/\mathcal{M})$ anomalies over the Northern
270 Hemisphere subtropics ($15^\circ\text{N}\text{-}25^\circ\text{N}$) and the T/M boundary latitude. The high correlation of 0.76
271 between them demonstrates that the T/M boundary migration is a corollary of T/M ratio changes
272 in the subtropical region.



254 **FIG. 4. Trends and interannual variability of the T/M boundary.** (a) Linear trends of $\log_{10}(\mathcal{T}/\mathcal{M})$ at each
 255 grid point. The Northern Hemispheric subtropics (15°N-25°N) are shown as the black dashed box. (b) Observed
 256 monthly time series of regional-mean $\log_{10}(\mathcal{T}/\mathcal{M})$ over the Northern Hemispheric subtropics (blue dashed)
 257 and ϕ_{TM} (black solid). One-year running mean is applied. Red line shows the theoretically-predicted ϕ_{TM} trend,
 258 and black line shows the observed trend by the least-squares best fit. The uncertainty shown as the gray shaded
 259 area is estimated as the 95 % confidence interval. (c) Regions with temporal-mean $\mathcal{T}/\mathcal{M} > 10$ calculated for
 260 July (top) and January (bottom) of 1982-1989 (blue) and 2017-2024 (red). (d) Sea surface temperature (SST)
 261 anomalies regressed on detrended ϕ_{TM} . (e) Observed monthly SST anomalies averaged over the Niño 3.4 region
 262 (5°S-5°N, 170°W-120°W; black solid box in (d)) and monthly zonal-mean ϕ_{TM} anomalies. One-year running
 263 mean is applied. (f) Theoretical (red) and observed (black) sensitivity of zonal-mean ϕ_{TM} to the eastern tropical
 264 Pacific SST anomalies (black dashed box in (d)). The uncertainty of the theoretical prediction (red shaded area)
 265 is estimated by assuming that the climate sensitivity is 1.5-4.5 °C/(2 × CO₂). The uncertainty of the observed
 266 trend (black shaded area) is the 95 % confidence interval.

273 To quantitatively understand the mechanism of global tropicalization, we decompose
274 $\log_{10}(\mathcal{T}/\mathcal{M})$ trends into contributions from \mathcal{T} and \mathcal{M} changes, according to:

$$\Delta(\log_{10}(\mathcal{T}/\mathcal{M})) = \Delta(\log_{10} \mathcal{T}) - \Delta(\log_{10} \mathcal{M}) \quad (7)$$

275 where Δ denotes trends or anomalies. This decomposition, shown in Supplementary Fig. 4, in-
276 dicates that the global tropicalization is primarily explained by the \mathcal{M} change resulting from cir-
277 culation weakening due to global warming³³. The small \mathcal{T} change is consistent with the Fixed
278 Anvil Temperature mechanism, where adjustment processes in cumulonimbus suppress changes
279 in radiative cooling rates under global warming³⁴.

280 Our simple model of the T/M boundary, when incorporating circulation weakening as de-
281 scribed by Held and Soden (2006)³³, predicts tropical expansion rates that agree with observed
282 values within the uncertainty range. Specifically, global circulation weakens approximately
283 $5\%/^{\circ}\text{C}$, which is estimated as the difference between water vapor change ($6.5\%/^{\circ}\text{C}$) following the
284 Clausius-Clapeyron relation and precipitation change ($1.5\%/^{\circ}\text{C}$) constrained by energy balance.
285 The theoretical tropical expansion rate obtained by reducing typical wind speed U_0 by $5\%/^{\circ}\text{C}$ in
286 equation (4) yields $0.24^{\circ}/(\text{decade})$ for the observed 0.8°C warming over 40 years (*see* Methods).
287 Figure 4b compares this theoretical trend with the observed trend, $0.14^{\circ} \pm 0.19^{\circ}/(\text{decade})$, which
288 is statistically insignificant but consistent with numerous prior studies²².

289 Although $0.24^{\circ}/(\text{decade})$ appears small, tropical expansion impacts are already apparent in some
290 seasons and regions. Figure 4c compares the tropical region during the first and last 8 years of
291 the analysis period for July (T/M boundary at maximum northward position) and January (maxi-
292 mum southward position). Tropical expansion is particularly pronounced in Asia-Oceania, where
293 Beijing and New Zealand newly fell into the tropical territory over the 40-year period. Trend sea-
294 sonality, evident in Fig. 3b and Supplementary Fig. 4d, further emphasizes tropical expansion

295 impacts (Northern Hemisphere July: $0.37^\circ/(\text{decade})$), allowing substantial updates to latitudinal
296 limits. Thus, many regions previously unexposed to tropical climate will face sudden onset of
297 tropical climate regimes in the near future.

298 *Interannual variations explained by the El Niño-Southern Oscillation*

299 The T/M boundary exhibits interannual variations in response to the El Niño-Southern Oscilla-
300 tion (ENSO), a prominent mode of climate variability on Earth. Figure 4d shows SST anomalies
301 regressed onto the T/M boundary latitude anomalies, with clear ENSO-characteristic patterns vis-
302 ible in the tropical Pacific. Figure 4e shows time series of the Niño 3.4 index, which characterizes
303 the ENSO phase, and the T/M boundary latitude, revealing large negative correlation of -0.70.
304 This negative correlation indicates that the T/M boundary migrates equatorward during El Niño
305 episodes and poleward during opposite-phase La Niña.

306 Because global-mean temperature tends to increase during El Niño^{35,36}, one may find this ENSO
307 response contradictory to global warming response. However, the T/M theory provides unified
308 understanding of this difference based on heating spatial patterns and circulation response. Under
309 global warming, circulation weakens due to constraints from water vapor transport accompanying
310 global temperature rise, reducing mechanical sources and expanding tropics. Under El Niño,
311 tropical eastern Pacific's local heating requires circulation intensification for heat redistribution,
312 increasing mechanical sources and contracting tropics (Supplementary Fig. 5). This mechanism
313 aligns with prior idealized atmospheric model studies, which showed that a broad heat source
314 expands the tropics in a global warming-like manner, whereas a narrow heat source contracts
315 tropics in an El Niño-like manner^{11,20,37}.

316 From this dynamical interpretation, the relationship between the eastern tropical Pacific SST
 317 increase and the circulation intensification can be estimated as follows:

$$\frac{dU_0}{dT} \sim \frac{R_d \rho_s L_v C_E U_{eq}}{8 C_v f U_0 m} \frac{dq_s}{dT} \approx 0.39 \text{ (m/s)/K} \quad (8)$$

318 (*see* Methods for details). Here, R_d is the gas constant for dry air, ρ_s is sea-level air density, L_v is
 319 latent heat, C_E is bulk exchange coefficient, U_{eq} is mean wind speed in the tropical eastern Pacific,
 320 and dq_s/dT is the temperature derivative of saturation specific humidity.

321 Transforming the ENSO circulation sensitivity into T/M boundary latitude sensitivity using
 322 equation (4), the theoretical value agrees with observations within the uncertainty range. Figure 4f
 323 compares this value with the observed sensitivity to tropical eastern Pacific SST. The T/M theory
 324 predicts that the Northern Hemisphere T/M boundary responds with sensitivity $-0.7^\circ \pm 0.1^\circ/\text{C}$
 325 in the tropical eastern Pacific, whereas least-squares estimation of observed sensitivity yields
 326 $-1.1^\circ \pm 0.4^\circ/\text{C}$.

327 **Conclusions**

328 The T/M theory provides a first-principles explanation of mechanisms that define the boundary
 329 between the tropics and the midlatitudes. The theory first establishes that the tropical region is
 330 where thermal source dominantly drives vertical motions, whereas the midlatitude region is where
 331 mechanical source also plays a significant role in determining vertical motions. The tropical-
 332 midlatitude boundary forms where mechanical sources become non-negligible, with a “phase tran-
 333 sition” between climate zones occurring in this boundary region. Our simple model describes the
 334 essential mechanism of the T/M boundary latitude determination. This idealized model provides
 335 unified understanding across different timescale phenomena, i.e., seasonal variability, tropical ex-
 336 pansion due to global warming, and the T/M boundary fluctuations forced by ENSO. Quantitative

337 consistency between theoretical predictions and observations for these phenomena supports the
338 validity of the T/M theory.

339 Singular phenomena emerge near the T/M boundary where thermal and mechanical source bal-
340 ance shifts delicately, forming a boundary layer region with unique characteristics. Within this
341 layer, cooperative thermal and mechanical adjustments produce mesoscale phenomena that con-
342 nect the two regions^{38,39}. For example, as the boundary region characteristics, stationary fronts
343 called “the Meiyu/Baiu front” emerge in June in East Asia; when crossing the boundary, tropi-
344 cal cyclones undergo extratropical transition. Furthermore, the presence of strong heat sources,
345 such as the warm ocean currents near the T/M boundary, creates regions where the tropics intrude
346 the midlatitudes. This “tropical spillover” plays roles in jet stream meridional migration^{40,41},
347 modulation of storm track zonal distribution⁴², and oceanic decadal-scale variations⁴³. In recent
348 years, the spatial resolution of observational data⁴⁴, general circulation models^{45,46}, and reanalysis
349 data⁴⁷ is rapidly increasing. With these advances, atmospheric behaviors within the T/M boundary
350 layer may be explainable as adjustment processes to balance the thermal and mechanical driving
351 sources.

352 The T/M theory brings direct implications for climate change mitigation. Most extreme weather
353 that threatens humanity, such as heavy rains, occurs via mesoscale phenomena. Therefore, under-
354 standing how large-scale constraints produce mesoscale phenomena is essential for disaster pre-
355 vention. In addition, physical understanding of the “tropical expansion” contributes to improving
356 future projection reliability for regional climate changes in the T/M boundary transit zones, where
357 approximately half the global population resides²². This “tropical expansion” forces societal in-
358 frastructure reconstruction through discontinuous changes to agriculture and water resources²³.
359 The physical robustness of the T/M theory is expected to guide the mitigation and adaptation

360 strategies for climate change^{15,21,22}, including the projected increase in wildfires and desertifica-
361 tion associated with the poleward expansion of subtropical dry zones^{23,48}.

362 The T/M theory also has implications for other scientific disciplines. For instance, since ter-
363 restrial climate boundaries serve as vegetation boundaries, the T/M theory provides theoretical
364 foundations for understanding shifts in habitable ranges for animals and plants^{28,29}. Meanwhile,
365 some migratory fishes move in opposite directions across the T/M boundary^{49,50}, suggesting the
366 T/M theory may help elucidate marine ecosystems. Furthermore, the T/M theory is applicable
367 to atmospheric circulation of other planets with different physical parameters (e.g., Mars)^{24,25}.
368 Comparison with other planets will offer a method to strengthen the plausibility of the theoretical
369 meteorology, aiding deeper understanding of Earth's atmosphere.

370 **References**

- 371 [1] Ryu Shimabukuro, Tomohiko Tomita, and Ken-ichi Fukui. Update of global maps of Alisov',
372 s climate classification. Prog. Earth Planet. Sci., 10(1):1–18, 2023.
- 373 [2] Zhe Li and Qinghua Ding. A global poleward shift of atmospheric rivers. Sci. Adv., 10(41):
374 eadq0604, 2024.
- 375 [3] Wolfgang Wicker, Emmanuele Russo, and Daniela IV Domeisen. A poleward storm track
376 shift reduces mid-latitude heatwave frequency: insights from an idealized atmospheric
377 model. Wea. Clim. Dyn., 6(3):965–979, 2025.
- 378 [4] Xiao Lu, Lin Zhang, Yuanhong Zhao, Daniel J Jacob, Yongyun Hu, Lu Hu, Meng Gao, Xiong
379 Liu, Irina Petropavlovskikh, Audra McClure-Begley, et al. Surface and tropospheric ozone
380 trends in the Southern Hemisphere since 1990: possible linkages to poleward expansion of
381 the Hadley circulation. Sci. Bull., 64(6):400–409, 2019.

- 382 [5] Wenmin Zhang, Guy Schurgers, Josep Peñuelas, Rasmus Fensholt, Hui Yang, Jing Tang,
383 Xiaowei Tong, Philippe Ciais, and Martin Brandt. Recent decrease of the impact of tropical
384 temperature on the carbon cycle linked to increased precipitation. Nat. Comm., 14(1):965,
385 2023.
- 386 [6] Nathan L Stephenson. Climatic control of vegetation distribution: the role of the water
387 balance. The American Naturalist, 135(5):649–670, 1990.
- 388 [7] I-Ching Chen, Jane K Hill, Ralf Ohlemüller, David B Roy, and Chris D Thomas. Rapid
389 range shifts of species associated with high levels of climate warming. Science, 333(6045):
390 1024–1026, 2011.
- 391 [8] Isaac M Held and Arthur Y Hou. Nonlinear axially symmetric circulations in a nearly invis-
392 cid atmosphere. J. Atmos. Sci., 37(3):515–533, 1980.
- 393 [9] Christopher C Walker and Tapio Schneider. Eddy influences on hadley circulations: Simula-
394 tions with an idealized gcm. J. Atmos. Sci., 63(12):3333–3350, 2006.
- 395 [10] Xavier J Levine and Tapio Schneider. Response of the hadley circulation to climate change
396 in an aquaplanet gcm coupled to a simple representation of ocean heat transport. J. Atmos.
397 Sci., 68(4):769–783, 2011.
- 398 [11] Xavier J Levine and Tapio Schneider. Baroclinic eddies and the extent of the Hadley circu-
399 lation: An idealized GCM study. J. Atmos. Sci., 72(7):2744–2761, 2015.
- 400 [12] Casey C Hilgenbrink and Dennis L Hartmann. The response of Hadley circulation extent
401 to an idealized representation of poleward ocean heat transport in an aquaplanet GCM. J.
402 Climate, 31(23):9753–9770, 2018.

- 403 [13] Hu Yang, Gerrit Lohmann, Xiaoxu Shi, and Juliane Müller. Evaluating the mechanism of
404 tropical expansion using idealized numerical experiments. Ocean-Land-Atmos. Res., 2:0004,
405 2023.
- 406 [14] Pengcheng Zhang, Nicholas J Lutsko, Spencer A Hill, and Shang-Ping Xie. Hadley cell
407 dynamics in an axisymmetric single-layer model: Effects of parameterized eddies and equa-
408 torial heating. J. Atmos. Sci., 82(12):2757–2770, 2025.
- 409 [15] Dian J Seidel, Qiang Fu, William J Randel, and Thomas J Reichler. Widening of the tropical
410 belt in a changing climate. Nature Geosci., 1(1):21–24, 2008.
- 411 [16] Osamu Miyawaki, Tiffany A Shaw, and Malte F Jansen. Quantifying energy balance regimes
412 in the modern climate, their link to lapse rate regimes, and their response to warming. J.
413 Climate, 35(3):1045–1061, 2022.
- 414 [17] Jian Lu, Gabriel A Vecchi, and Thomas Reichler. Expansion of the Hadley cell under global
415 warming. Geophysical Research Letters, 34(6), 2007.
- 416 [18] Dargan MW Frierson, Jian Lu, and Gang Chen. Width of the hadley cell in simple and
417 comprehensive general circulation models. Geophys. Res. Lett., 34(18), 2007.
- 418 [19] PF Freisen, JM Arblaster, C Jakob, and JM Rodríguez. Investigating tropical versus extrat-
419 ropical influences on the southern hemisphere tropical edge in the unified model. J. Geophys.
420 Res. Atmos., 127(7):e2021JD036106, 2022.
- 421 [20] Polina Khapikova and Tapio Schneider. An energetic framework for understanding Hadley
422 circulation width variations: Seasonal cycle, ENSO, and global warming. J. Atmos. Sci., 82
423 (11):2569–2580, 2025.

- 424 [21] Qiang Fu, Celeste M Johanson, John M Wallace, and Thomas Reichler. Enhanced mid-
425 latitude tropospheric warming in satellite measurements. Science, 312(5777):1179–1179,
426 2006.
- 427 [22] Paul W Staten, Jian Lu, Kevin M Grise, Sean M Davis, and Thomas Birner. Re-examining
428 tropical expansion. Nature Climate Change, 8(9):768–775, 2018.
- 429 [23] Natalie J Burls, Ross C Blamey, Benjamin A Cash, Erik T Swenson, Abdullah al Fahad,
430 Mary-Jane M Bopape, David M Straus, and Chris JC Reason. The Cape Town “ day zero ”
431 drought and Hadley cell expansion. Npj Clim. Atmos. Sci., 2(1):27, 2019.
- 432 [24] PL Read. Dynamics and circulation regimes of terrestrial planets. Planet. Space Sci., 59(10):
433 900–914, 2011.
- 434 [25] Adam P Showman, Robin D Wordsworth, Timothy M Merlis, and Yohai Kaspi. Atmospheric
435 circulation of terrestrial exoplanets. Comp. Climatol. Terr. Planets, 1:277–326, 2013.
- 436 [26] Haoyu Tong, Tim Li, and Xiao Pan. Meridional shift of climatological tropical cyclone
437 genesis location in the western North Pacific. Atmos. Sci. Lett., 25(11):e1263, 2024.
- 438 [27] Courtney Schumacher and Aaron Funk. Assessing convective-stratiform precipitation
439 regimes in the tropics and extratropics with the GPM satellite radar. Geophys. Res. Lett.,
440 50(14):e2023GL102786, 2023.
- 441 [28] Marten Scheffer, Steve Carpenter, Jonathan A Foley, Carl Folke, and Brian Walker. Catastrophic
442 shifts in ecosystems. Nature, 413(6856):591–596, 2001.
- 443 [29] Gian-Reto Walther, Eric Post, Peter Convey, Annette Menzel, Camille Parmesan, Trevor JC
444 Beebe, Jean-Marc Fromentin, Ove Hoegh-Guldberg, and Franz Bairlein. Ecological re-
445 sponses to recent climate change. Nature, 416(6879):389–395, 2002.

- 446 [30] Adam H Sobel, Johan Nilsson, and Lorenzo M Polvani. The weak temperature gradient
447 approximation and balanced tropical moisture waves. *J. Atmos. Sci.*, 58(23):3650–3665,
448 2001.
- 449 [31] Jule G Charney and NA Phillips. Numerical integration of the quasi-geostrophic equations
450 for barotropic and simple baroclinic flows. *J. Atmos. Sci.*, 10(2):71–99, 1953.
- 451 [32] Piers M. Forster, Trude Storelvmo, Kyle C. Armour, William Collins, Jean-Louis Dufresne,
452 David Frame, Daniel J. Lunt, Thorsten Mauritsen, Matthew D. Palmer, Masahiro Watan-
453 abe, Martin Wild, and Huan Zhang. The Earth ’ s energy budget, climate feedbacks, and
454 climate sensitivity. In Valérie Masson-Delmotte, Panmao Zhai, Anna Pirani, Sarah L. Con-
455 nors, Clotilde Péan, Sophie Berger, Nada Caud, Yang Chen, Leah Goldfarb, Melinda I.
456 Gomis, Mengtian Huang, Katherine Leitzell, Elisabeth Lonnoy, J. B. Robin Matthews,
457 Thomas K. Maycock, Tim Waterfield, Ozge Yelekçi, Rong Yu, and Bohan Zhou, edi-
458 tors, *Climate Change 2021: The Physical Science Basis*, pages 923–1054. Cambridge
459 University Press, Cambridge, United Kingdom and New York, NY, USA, 2021. doi:
460 10.1017/9781009157896.009.
- 461 [33] Isaac M Held and Brian J Soden. Robust responses of the hydrological cycle to global
462 warming. *J. Climate*, 19(21):5686–5699, 2006.
- 463 [34] Dennis L Hartmann and Kristin Larson. An important constraint on tropical cloud-climate
464 feedback. *Geophys. Res. Lett.*, 29(20):12–1, 2002.
- 465 [35] Yu Kosaka and Shang-Ping Xie. Recent global-warming hiatus tied to equatorial Pacific
466 surface cooling. *Nature*, 501(7467):403–407, 2013.

- 467 [36] Yu Kosaka and Shang-Ping Xie. The tropical Pacific as a key pacemaker of the variable rates
468 of global warming. Nature Geosci., 9(9):669–673, 2016.
- 469 [37] Neil F Tandon, Edwin P Gerber, Adam H Sobel, and Lorenzo M Polvani. Understanding
470 Hadley cell expansion versus contraction: Insights from simplified models and implications
471 for recent observations. J. Climate, 26(12):4304–4321, 2013.
- 472 [38] Ryosuke Shibuya, Yukari Takayabu, and Hiroataka Kamahori. Dynamics of widespread ex-
473 treme precipitation events and the associated large-scale environment using AMeDAS and
474 JRA-55 data. J. Climate, 34(22):8955–8970, 2021.
- 475 [39] Yu-Xiang Qiao, Hirohiko Nakamura, and Tomohiko Tomita. Warming of the kuroshio cur-
476 rent over the last four decades has intensified the meiyu-baiu rainband. Geophys. Res. Lett.,
477 51(2):e2023GL107021, 2024.
- 478 [40] Tsubasa Kohyama, Yoko Yamagami, Hiroaki Miura, Shoichiro Kido, Hiroaki Tatebe, and
479 Masahiro Watanabe. The Gulf stream and Kuroshio current are synchronized. Science, 374
480 (6565):341–346, 2021.
- 481 [41] Tsubasa Kohyama, Yoko Yamagami, Shoichiro Kido, Fumiaki Ogawa, and Hiroaki Miura.
482 Interactive annular mode links jet stream-ocean coupling to decadal Northern Hemispheric
483 warmth. 2025.
- 484 [42] Brian J Hoskins and Paul J Valdes. On the existence of storm-tracks. J. Atmos. Sci., 47(15):
485 1854–1864, 1990.
- 486 [43] Robert CJ Wills, David S Battisti, Cristian Proistosescu, LuAnne Thompson, Dennis L Hart-
487 mann, and Kyle C Armour. Ocean circulation signatures of north pacific decadal variability.
488 Geophys. Res. Lett., 46(3):1690–1701, 2019.

- 489 [44] Boyin Huang, Chunying Liu, Viva Banzon, Eric Freeman, Garrett Graham, Bill Hankins,
490 Tom Smith, and Huai-Min Zhang. Improvements of the daily optimum interpolation sea
491 surface temperature (DOISST) version 2.1. Journal of Climate, 34(8):2923–2939, 2021.
- 492 [45] Hirofumi Tomita and Masaki Satoh. A new dynamical framework of nonhydrostatic global
493 model using the icosahedral grid. Fluid Dynamics Research, 34(6):357, 2004.
- 494 [46] Ryusuke Masunaga, Tomoki Miyakawa, Takao Kawasaki, and Hisashi Yashiro. Flux adjust-
495 ment on seasonal-scale sea surface temperature drift in NICOCO. J. Meteor. Soc. Japan, 101
496 (3):175–189, 2023.
- 497 [47] Hans Hersbach, Bill Bell, Paul Berrisford, Shoji Hirahara, András Horányi, Joaquín Muñoz-
498 Sabater, Julien Nicolas, Carole Peubey, Raluca Radu, Dinand Schepers, et al. The era5 global
499 reanalysis. Quarterly journal of the royal meteorological society, 146(730):1999–2049, 2020.
- 500 [48] Paul W Staten, Kevin M Grise, Sean M Davis, Kristopher B Karnauskas, Darryn W Waugh,
501 Amanda C Maycock, Qiang Fu, Kerry Cook, Ori Adam, Isla R Simpson, et al. Tropical
502 widening: From global variations to regional impacts. Bull. Amer. Meteor. Soc., 101(6):
503 E897–E904, 2020.
- 504 [49] Minato Yasui and Noriyoshi Mori. The route of skipjack tuna (*Katsuwonus Pelamis*) in their
505 migration into the coastal waters of Japan, as seen from, tagging results. Bull. Shizuoka Pref.
506 Fish. Exp. Stn., 20:1–8, 1985.
- 507 [50] S Ito, M Ogura, T Tanabe, K Takeuchi, and M Nonaka. Estimation of the skipjack [*katsu-*
508 *wonus pelamis*] migration pattern by a skipjack general migration model. Bull. Tohoku Natl.
509 Fish. Res. Inst., 60:41–48, 1998.

- 510 [51] James R Holton and Gregory J Hakim. An introduction to dynamic meteorology, volume 88.
511 Academic press, 2013.
- 512 [52] Christopher S Bretherton, Martin Widmann, Valentin P Dymnikov, John M Wallace, and
513 Ileana Bladé. The effective number of spatial degrees of freedom of a time-varying field. J.
514 Climate, 12(7):1990–2009, 1999.
- 515 [53] Lixin Wu, Wenju Cai, Liping Zhang, Hisashi Nakamura, Axel Timmermann, Terry Joyce,
516 Michael J McPhaden, Michael Alexander, Bo Qiu, Martin Visbeck, et al. Enhanced warming
517 over the global subtropical western boundary currents. Nature Climate Change, 2(3):161–
518 166, 2012.
- 519 [54] Guang Jun Zhang and Michael J McPhaden. The relationship between sea surface tempera-
520 ture and latent heat flux in the equatorial Pacific. J. Climate, 8(3):589–605, 1995.
- 521 [55] WG Large and S Pond. Open ocean momentum flux measurements in moderate to strong
522 winds. J. Phys. Oceanogr., 11(3):324–336, 1981.

523 **Methods**

524 **Scaling of \mathcal{T}/\mathcal{M} applicable for the Earth’s large-scale system**

525 This section demonstrates that the scaling $\mathcal{T}/\mathcal{M} \sim J/(fU^2L_R^2/L^2)$ shown on the right-hand side
526 of equation (2) holds by requiring two properties characterizing Earth’s large-scale phenomena:
527 hydrostatic balance and quasi-geostrophic balance. Here, we assume the Northern Hemisphere
528 with positive Coriolis parameter, though the same argument applies to the Southern Hemisphere
529 by replacing f with $-f$. Below, we denote scales of physical variables by curly braces $\{\}$, and \sim
530 means “equal in scale.”

531 From the definition introduced in equation (2):

$$\mathcal{T}/\mathcal{M} := \left| \frac{[j]}{[-C_p DT/Dt]} \right| = \left| \frac{[j]}{-C_p D[T]/Dt} \right| \quad (9)$$

532 Using the hypsometric equation based on hydrostatic balance:

$$Z_T = \frac{R_d [T]}{g} \ln \frac{p_1}{p_2} \quad (10)$$

533 we can eliminate $[T]$ from equation (9) to obtain:

$$\mathcal{T}/\mathcal{M} = \left| \frac{[j]}{[-g(C_p)/(R_d \ln \frac{p_1}{p_2}) \cdot DZ_T/Dt]} \right| \simeq \left| \frac{[j]}{-g DZ_T/Dt} \right| \quad (11)$$

534 using $C_p/(R_d \ln \frac{p_1}{p_2}) = 7/(2 \ln 10) \sim 1$.

535 From the continuity equation, DZ_T/Dt can be expressed as:

$$\left\{ \frac{DZ_T}{Dt} \right\} \sim H \{ \delta \} \quad (12)$$

536 where $\{ \delta \}$ is divergence and H is typical tropospheric height. Furthermore, under quasi-
 537 geostrophic balance, which is valid when Rossby number $Ro := U/fL$ is small (widely applicable
 538 to large-scale phenomena with $L \gtrsim 2000$ km, except near the equator; Supplementary Fig. 2), the
 539 divergence scale is $\{ \delta \} \sim RoU/L$ (see Supplementary Text 2). Thus,

$$\left\{ \frac{DZ_T}{Dt} \right\} \sim H \cdot Ro \frac{U}{L} \sim \frac{HU^2}{fL^2} \quad (13)$$

540 Using this with equation (11), the scale of \mathcal{T}/\mathcal{M} becomes:

$$\{ \mathcal{T}/\mathcal{M} \} \sim \frac{J}{fU^2 \cdot gH/f^2L^2} \sim \frac{J}{fU^2} \cdot \frac{L^2}{L_R^2} \quad (14)$$

541 where we define $L_R := \sqrt{gH}/f$. Since our main goal is to understand the importance of physical
 542 processes through scaling analysis rather than to compute precise local values, we hereafter use
 543 \mathcal{T} and \mathcal{M} without curly braces to denote their scales for simplicity.

544 **Simplest theoretical model to predict the T/M boundary latitude**

545 In the main text, we construct a static model shown in Fig. 1 to extract the essence of the T/M
546 boundary. This simple model allows us to describe the first-principles mechanism to determine
547 the T/M boundary latitude to the first order.

548 *General idea*

549 As described in the main text, we choose a horizontal scale satisfying $L \sim \sqrt{10}L_R$ as a reasonable
550 coarse-graining to resolve the T/M boundary, and reduce the T/M boundary condition $\mathcal{T}/\mathcal{M} \sim 10$
551 to the simple condition $J \sim fU^2$. Using this condition, we derive the T/M boundary latitude as
552 follows.

553 First, we estimate the scale of diabatic heating $J(\phi)$ as a function of latitude ϕ , based on the
554 difference between shortwave radiation (SW) received from the sun and longwave radiation (LW)
555 lost to space. We assume that net radiative heating received by Earth (SW-LW) becomes an atmo-
556 spheric heat source through either shortwave absorption by the atmosphere or sensible and latent
557 heat fluxes from the surface. When net radiative heating is negative, it cools the atmosphere. In
558 reality, approximately one-tenth of incident energy is transported by oceans, but as a zeroth-order
559 approximation, we neglect ocean heat transport. Since solar zenith angle increases from equator to
560 pole, SW decreases with the cosine of latitude. We assume that heat received by the atmosphere is
561 homogenized through the large-scale atmospheric circulation on timescales much faster than the
562 climate time scale, and thus, we use the global mean value for LW. In reality, LW also varies with
563 latitude, but much more gradually than SW spatial variations.

564 Next, we estimate $f(\phi)U(\phi)^2$ as a function of latitude. Coriolis parameter $f(\phi)$ increases from
565 equator to pole with the sine of latitude. Wind speed $U(\phi)$ also varies with latitude, but we specify
566 $U_0 := U(\phi_{TM})$ as the model input representing the typical wind speed at the T/M boundary. By

567 this specification, we are also prescribing eddy viscosity in the model. In this study, for example,
 568 we have adopted $U_0 = 10$ m/s as the traditional scaling parameter for a representative tropospheric
 569 wind speed⁵¹. In any case, our model is not intended to precisely predict the climatological T/M
 570 boundary latitude, but rather to understand the essential mechanism behind its determination.

571 Finally, the equation $J(\phi) = f(\phi)U(\phi)^2$ yields two analytical solutions in $0 < \phi < \pi/2$. The
 572 solution closer to the equator, ϕ_{TM} , represents the T/M boundary latitude. The other solution ϕ_{MP} ,
 573 whose existence is predicted a priori, represents the boundary between the midlatitude and polar
 574 (M/P) regions. The following subsections explain these procedures mathematically.

575 *Derivation of $J(\phi)$ and $f(\phi)U(\phi)^2$*

576 First, we derive the expression for $J(\phi)$. The SW energy flux received by the atmosphere at
 577 latitude ϕ , denoted $F^\downarrow(\phi)$, can be expressed using the equatorial value $F_0 := F^\downarrow(0)$ as $F^\downarrow(\phi) =$
 578 $F_0 \cos \phi$. Due to the radiative equilibrium, the global-mean LW, denoted $\overline{F^\uparrow}$, equals the global-
 579 mean SW:

$$\overline{F^\uparrow} = \frac{1}{4\pi R^2} \int_{-\pi/2}^{\pi/2} \int_0^{2\pi} (F_0^\downarrow \cos \phi) R^2 \cos \phi d\lambda d\phi \implies \overline{F^\uparrow} = \frac{\pi}{4} F_0 \quad (15)$$

580 where R is the Earth's radius and λ is longitude. Therefore, diabatic heating per unit mass $J(\phi)$ is:

$$mJ(\phi) = |F^\downarrow(\phi) - \overline{F^\uparrow}| \implies J(\phi) = \left| \frac{F_0}{m} \cos \phi - \frac{\pi F_0}{4 m} \right| \quad (16)$$

581 where m is the vertically-integrated atmospheric mass per unit area.

582 Then, $f(\phi)U(\phi)^2$ is expressed by substituting the Coriolis parameter definition:

$$f(\phi)U(\phi)^2 = 2\Omega \sin \phi (U(\phi))^2 \quad (17)$$

583 Analytical solution of $J(\phi) = f(\phi)U(\phi)^2$

584 Using the above expressions, the T/M boundary condition $J(\phi) = f(\phi)U(\phi)^2$ yields:

$$\left| \frac{F_0}{m} \cos \phi - \frac{\pi F_0}{4 m} \right| = 2\Omega \sin \phi (U(\phi))^2 \quad (18)$$

585 First, we consider the case where $SW > LW$, i.e., the argument of the absolute value is positive.

586 Denoting this solution ϕ_{TM} and setting $U_0 := U(\phi_{TM})$:

$$\frac{F_0}{m} \cos \phi_{TM} - \frac{\pi F_0}{4 m} = 2\Omega \sin \phi_{TM} U_0^2 \quad (19)$$

$$\iff -2\Omega U_0^2 \sin \phi_{TM} + \frac{F_0}{m} \cos \phi_{TM} = \frac{\pi F_0}{4 m} \quad (20)$$

$$\iff \sqrt{4\Omega^2 U_0^4 + \frac{F_0^2}{m^2}} \sin \left(\phi_{TM} - \arctan \left(\frac{F_0}{2\Omega U_0^2 m} \right) \right) = \frac{\pi F_0}{4 m} \quad (21)$$

$$\iff \phi_{TM} = \arctan \left(\frac{F_0}{2\Omega U_0^2 m} \right) - \arcsin \left(\frac{\pi F_0}{4 \sqrt{4\Omega^2 m^2 U_0^4 + F_0^2}} \right) \quad (22)$$

587 Under radiative equilibrium, the relation among longwave radiation $\overline{F^\uparrow} = \pi F_0/4$, solar constant

588 S_0 , and mean planetary albedo A is:

$$S_0(1-A) \cdot \pi R^2 = \overline{F^\uparrow} \cdot 4\pi R^2 \implies F_0 = \frac{S_0(1-A)}{\pi} \quad (23)$$

589 The analytical solution for ϕ_{TM} is thus:

$$\phi_{TM}(U_0) = \arctan \left(\frac{S_0(1-A)}{2\Omega U_0^2 \pi m} \right) - \arcsin \left(\frac{S_0(1-A)}{4m \sqrt{4\Omega^2 U_0^4 + S_0^2(1-A)^2/\pi^2 m^2}} \right) \quad (24)$$

590 where $S_0 = 1,366 \text{ W/m}^2$, $A = 0.3$, $m = 10,337 \text{ kg/m}^2$. For example, if we adopt $U_0 = 10 \text{ m/s}$ as

591 a model input, the model yields $\phi_{TM} \simeq 19.0^\circ$.

592 Next, we consider the case where $SW < LW$, i.e., the argument of the absolute value is negative.

593 Denoting this solution ϕ_{MP} , we analytically obtain:

$$\phi_{MP}(U_0) = \pi - \arctan \left(\frac{S_0(1-A)}{2\Omega U_0^2 \pi m} \right) - \arcsin \left(\frac{S_0(1-A)}{4m \sqrt{4\Omega^2 U_0^4 + S_0^2(1-A)^2/\pi^2 m^2}} \right) \quad (25)$$

594 This latitude ($\phi_{MP} \simeq 71.5^\circ$) is inappropriate as a T/M boundary solution, but represents the bound-
 595 ary between midlatitude and polar regions (M/P boundary) where radiative cooling and available
 596 potential energy conversion are equally important. However, in the Earth’s polar regions, the M/P
 597 boundary appears less distinctly than the T/M boundary, likely due to large noise from lateral and
 598 lower boundary conditions.

599 **Observational validation**

600 *Data*

601 We have used the reanalysis data from the European Centre for Medium-Range Weather Fore-
 602 casts Reanalysis version 5 (ERA5)⁴⁷, whose time span covers from 1982 through 2024. Spatial
 603 resolution is 0.25° in both longitude and latitude directions. The vertically-averaged diabatic heat-
 604 ing rate per unit mass is calculated as:

$$[j] = \frac{Q_{\text{rad}} + \text{LH} + \text{SH} - L_v \nabla \cdot [\vec{F}_v]}{m} \quad (26)$$

605 Here, radiative heating per unit area Q_{rad} is obtained by subtracting net radiation reaching the
 606 surface from net radiation reaching the top of atmosphere for both longwave and shortwave (ERA5
 607 uses downward positive sign convention). LH and SH are obtained by applying negative signs to
 608 the downward latent and sensible heat flux data from the atmosphere to the surface provided per
 609 unit area. Since ERA5 provides vertically-integrated moisture divergence $\nabla \cdot [\vec{F}_v]$ (hereafter []
 610 denotes vertical integration), we multiplied by latent heat $L_v = 2.5 \times 10^6$ J/kg to obtain horizontal
 611 latent heat transport $L_v \nabla \cdot [\vec{F}_v]$. The constant $m = [\rho]$ (ρ denotes density), the vertical integral of
 612 mass of atmosphere provided by ERA5, is used to convert per-unit-area to per-unit-mass quantities.

613 The J and fU^2 used for \mathcal{T}/\mathcal{M} calculation are obtained as follows. For J , we take the absolute
614 value of $[j]$ calculated from equation (26). For fU^2 :

$$f = 2\Omega \sin \phi \quad (27)$$

615

$$U = [u] = \frac{1}{m} \sqrt{([\rho u])^2 + ([\rho v])^2} \quad (28)$$

616 using the Earth's angular velocity $\Omega = 7.2 \times 10^{-4}$ /s, with $[u]$ obtained by dividing the magnitude
617 of vertically-integrated mass flux, which is also provided by ERA5, by m .

618 Observed sea surface temperature (SST) data in Fig. 4c, 4d, and 4e are obtained from the
619 National Oceanic and Atmospheric Administration (NOAA) Optimal Interpolation SST (OISST)
620 version 2 high-resolution dataset⁴⁴. Spatial resolution was interpolated to 1° in both zonal and
621 meridional directions for computational efficiency. The time span used in this study is from 1982
622 through 2024.

623 *Statistical methods*

624 Monthly climatology is calculated by averaging each variable for each calendar month. For anal-
625 yses of monthly anomalies, the corresponding monthly climatology and linear trends are removed,
626 except in the analysis of the global warming response, for which the linear trend is retained. The
627 statistical significance of correlations and regressions is assessed using a two-tailed Student's t-
628 test. To account for autocorrelation in the time series when estimating the effective degrees of
629 freedom, we employ the formula proposed by Bretherton et al. (1999)⁵². The Niño 3.4 index
630 is calculated as the regional-mean detrended SST anomalies over the Niño 3.4 region (5°N – 5°S ,
631 170°W – 120°W).

632 “Virtual lighting” visualization of the geopotential height surface

633 Figure 2a shows shaded “relief” of the 500 hPa geopotential height surface with “virtual light-
634 ing” cast from a specific angle. This visualization technique, devised by the third author, produces
635 spatial shading variations according to the gradient direction of the geopotential height surface at
636 each point. Specifically, shading is configured to brighten if the dot product between the unit gradi-
637 ent vector and (2, -1) is large, such that slopes dipping from roughly southeast to northwest appear
638 bright, whereas those dipping from northwest to southeast appear dark. This shading presents the
639 “relief” of the geopotential height field three-dimensionally, offering a fine view of flow patterns
640 that are difficult to visualize using standard contour plots.

641 **Atmospheric low-pass filter**

642 As shown in the main text, the maximum northward T/M boundary migration occurs not in
643 June, when solar radiation is strongest, but approximately one month later in July. We attribute
644 this response lag to the atmospheric heat capacity and the climate sensitivity (temperature rise per
645 W/m^2 radiative forcing), constructing the following “atmospheric low-pass filter”:

$$\gamma m C_p \frac{d\phi_{TM,out}(t)}{dt} + \phi_{TM,out}(t) = \phi_{TM,in}(t) \quad (29)$$

646 where $\phi_{TM,in}(t)$ is the T/M boundary latitude anomaly before filtering, derivable theoretically by
647 introducing seasonal radiation variations into the simple model (detailed later). $\phi_{TM,out}(t)$ is the
648 T/M boundary latitude anomaly after filtering, reproducing observed seasonal variations. The
649 climate sensitivity γ has units $K/(W/m^2)$ (inverse of the conventionally-used climate feedback
650 parameter λ_c). C_p ($= 1,004 J/(kg \cdot K)$) is the specific heat at constant pressure for dry air, and m
651 is vertically-integrated atmospheric mass per unit area as already used. The product $\gamma m C_p$ gives a
652 time constant of this system with dimensions of time (units: s).

653 The atmospheric filter equation (29) can be derived as follows. For the region near the T/M
 654 boundary, the radiative budget equation gives:

$$mC_p \frac{d\Delta T(t)}{dt} = \Delta F_{\text{TM}}^\downarrow(t) - \lambda_c \Delta T(t) \quad (30)$$

655 where $\Delta F_{\text{TM}}^\downarrow(t)$ is the seasonal variation of shortwave radiation in this region, and $\lambda_c \Delta T(t)$ is the
 656 longwave feedback for a given temperature anomaly $\Delta T(t)$. Then, we assume that the T/M bound-
 657 ary latitude anomaly after filtering $\phi_{\text{TM},\text{out}}$ is proportional to the temperature anomaly $\Delta T(t)$, or
 658 $\phi_{\text{TM},\text{out}} = k\Delta T(t)$, where k is a constant. This proportionality is the first-order approximation
 659 of the warming response of the T/M boundary latitude as discussed in the main text. Similarly,
 660 $\phi_{\text{TM},\text{in}}(t) = k\Delta F_{\text{TM}}^\downarrow(t)/\lambda_c$, meaning that $\phi_{\text{TM},\text{in}}(t)$ is the T/M boundary latitude anomaly corre-
 661 sponding to the radiative-equilibrium temperature, which is derived by not accounting for the tran-
 662 sience of the Earth's atmosphere. Substituting $\Delta T(t) = \phi_{\text{TM},\text{out}}/k$ and $\Delta F_{\text{TM}}^\downarrow(t) = \lambda_c \phi_{\text{TM},\text{in}}(t)/k$
 663 into equation (30), we obtain equation (29), considering that $\gamma = 1/\lambda_c$.

664 The atmospheric low-pass filter can be understood through analogy with the RC low-pass filter
 665 circuit shown in Fig. 3c. For an RC low-pass filter circuit with input voltage $V_{\text{in}}(t)$ and output
 666 voltage $V_{\text{out}}(t)$, Kirchoff's second law gives:

$$RC \frac{dV_{\text{out}}(t)}{dt} + V_{\text{out}}(t) = V_{\text{in}}(t) \quad (31)$$

667 Therefore, the climate sensitivity γ (the atmospheric heat capacity mC_p) corresponds to the resis-
 668 tance R (the capacitance C), so the time constant of the climate response γmC_p plays the same role
 669 as that of the filter RC , i.e., the e-folding time for a step function input.

670 The latitude $\phi_{\text{TM},\text{in}}(t)$ before filtering reaches its maximum in June and minimum in December,
 671 with meridional migration amplitude exceeding observations. Figure 3d's blue dashed line shows
 672 $\phi_{\text{TM},\text{in}}(t)$ obtained by modifying equation (18) to include seasonal radiation variations:

$$\frac{F_0}{m} (h_0 \sin \phi \sin \delta + \cos \phi \cos \delta \sin h_0) - \frac{\pi F_0}{4 m} = 2\Omega \sin \phi (U(\phi))^2 \quad (32)$$

673 where monthly-mean solar declination δ and hour angle h_0 at latitude ϕ are obtained from:

$$\delta := -23.44^\circ \cos\left(\frac{2\pi}{365}(N+10)\right) \quad (33)$$

674

$$h_0 := \arccos(-\tan\phi \tan\delta) \quad (34)$$

675 Here, N is the day of year. Since we focus on seasonal variations, we correct the bias from annual
 676 climatology. However, $\phi_{TM,in}(t)$ obtained this way does not accurately reproduce observed ϕ_{TM}
 677 behavior (Fig. 3d, black line).

678 In contrast, the latitude $\phi_{TM,out}(t)$ after passing through the filter reproduces observations well.
 679 The red line in Fig. 3d shows the theoretical prediction of $\phi_{TM,out}(t)$ estimated using climate
 680 sensitivity according to IPCC AR6³² as “3°C temperature increase for doubling CO₂ forcing (3.7
 681 W/m²)”. This theoretical value is obtained as follows. First, we subtract the time-mean value
 682 $\overline{\phi_{TM,in}}$ from the time series of $\phi_{TM,in}(t)$, and perform the Fourier transform to obtain $\hat{\phi}_{TM,in}(\omega)$.
 683 Then, we input $\hat{\phi}_{TM,in}(\omega)$ into the Fourier-transformed version of equation (29):

$$\hat{\phi}_{TM,out}(\omega) = \frac{1}{1 + i\omega(\gamma m C_p)} \hat{\phi}_{TM,in}(\omega) \quad (35)$$

684 Finally, we take the inverse Fourier transform of the output $\hat{\phi}_{TM,out}(\omega)$, and add back the time-
 685 mean value $\overline{\phi_{TM,in}}$. The shaded region in Fig. 3 indicates the theoretical prediction range for
 686 $\phi_{TM,out}(t)$, which is estimated by assuming the uncertainty range of the climate sensitivity to be
 687 1.5–4.5°C/(2×CO₂). This “atmospheric low-pass filter” delays the phase of seasonal variations by
 688 approximately one month, and attenuates the amplitude to about 65–85%. As a result, the theoret-
 689 ical prediction of T/M boundary latitude exhibits seasonal variations consistent with observations.

690 **Theoretical considerations for the warming response of T/M ratio**

691 Here we show the method for estimating the warming response of the T/M boundary using the
 692 simple model presented in the main text. Following Held and Soden (2006)³³, circulation changes

693 under global warming are estimated as the difference between water vapor change rate (6.5%/K)
 694 following the Clausius-Clapeyron relation and precipitation change rate (1.5%/K) constrained by
 695 energy conservation, yielding approximately 5%/K global weakening. Substituting reduced typi-
 696 cal wind speed $U_0 + \Delta U_0 = 9.5$ m/s ($\Delta U_0 < 0$) into equation (5):

$$\begin{aligned} \phi_{\text{TM}}(U_0 + \Delta U_0) &= \arctan\left(\frac{S_0(1-A)}{2\Omega(U_0 + \Delta U_0)^2 \pi m}\right) - \arcsin\left(\frac{S_0(1-A)}{4m\sqrt{4\Omega^2(U_0 + \Delta U_0)^4 + S_0^2(1-A)^2/\pi^2 m^2}}\right) \quad (36) \\ &\simeq 20.2^\circ \quad (37) \end{aligned}$$

697 Thus, the poleward shift of the T/M boundary per kelvin of global warming is:

$$\frac{d\phi_{\text{TM}}(U_0)}{dT} \simeq \frac{\phi_{\text{TM}}(U_0 + \Delta U_0) - \phi_{\text{TM}}(U_0)}{\Delta T} = \frac{20.2^\circ - 19.0^\circ}{1 \text{ K}} = 1.2^\circ/\text{K} \quad (38)$$

698 Hence, the 0.8 K global warming over the past 40 years yields the tropical expansion rate of
 699 $1.2^\circ/\text{K} \times 0.8 \text{ K}/(40 \text{ yr}) = 0.24^\circ/\text{decade}$.

700 Note that the above discussion is based on global means, so this method cannot necessarily be
 701 used for explaining local trends. Indeed, tropical expansion has several exception regions. Over
 702 western boundary current regions, expansion occurs but circulation weakening does not solely
 703 dominate. The recent strengthening of western boundary currents⁵³ means that T/M changes from
 704 increased diabatic heating from lower boundary contribute comparably to \mathcal{M} changes. Addition-
 705 ally, only on the polar side of jet streams does the T/M ratio show opposite tendencies with weak
 706 “midlatitudinalization” rather than tropicalization. This opposite response is because the poleward
 707 jet shift enhances the circulation in this region, offsetting the increased diabatic heating effects
 708 (*see also* Supplementary Fig. 4).

709 **Theoretical considerations for the sensitivity of \mathcal{T}/\mathcal{M} to ENSO**

710 Here we derive the T/M boundary sensitivity to ENSO presented in equation (8) of the main
 711 text. When El Niño occurs, the eastern equatorial Pacific SST rises with accompanying upward

712 surface heat flux anomalies, which warms the entire tropical region due to the WTG characteris-
713 tics. However, because this fast response of heating is confined in the tropical region, the slower
714 atmospheric circulation then transports most of the heat poleward. Therefore, we assume that all
715 of the heat associated with the El Niño event is used for circulation intensification (increasing
716 \mathcal{M}), rather than for increasing \mathcal{T} in the T/M boundary region. This assumption is consistent with
717 Supplementary Fig. 5, which shows that the T/M response to ENSO is primarily explained as the
718 \mathcal{M} response.

719 Based on this assumption, the tropical heating per unit mass balances poleward heat transport:

$$J \sim C_v U_0 \left\{ \frac{dT}{dy} \right\} \quad (39)$$

720 where C_v is the specific heat at constant volume for dry air. Meanwhile, due to the small Rossby
721 number, thermal wind balance constrains meridional temperature gradient:

$$U_0 \sim \frac{R_d}{f} \left\{ \frac{dT}{dy} \right\} \quad (40)$$

722 where R_d is the gas constant for dry air. Therefore, the tropical heating is estimated as:

$$J \sim \frac{C_v f}{R_d} U_0^2 \quad (41)$$

723 When ENSO-induced eastern tropical Pacific SST anomaly dT increases tropical heating by dJ
724 and typical wind speed by dU_0 , differentiating equation (41) with respect to T :

$$\frac{dJ}{dT} \sim \frac{2C_v f U_0}{R_d} \frac{dU_0}{dT} \quad (42)$$

725 Thus, ENSO-induced circulation (typical wind speed) change is:

$$\frac{dU_0}{dT} \sim \frac{R_d}{2C_v f U_0} \frac{dJ}{dT} \quad (43)$$

726 Next, we obtain this heating from local SST warming. When the tropical eastern Pacific SST
727 increases 1 K as a regional-mean value, local atmospheric latent heat flux change dJ_{local}/dT can

728 be estimated by bulk formula:

$$m \frac{dJ_{\text{local}}}{dT} = \rho_s L_v C_E U_{\text{eq}} \frac{dq_s}{dT} \simeq 38.0 \text{ (W/m}^2\text{)}/\text{K} \quad (44)$$

729 which agrees with observations to the first order⁵⁴. Here, we use the surface air density $\rho_s =$
 730 1.2 kg/m^3 , latent heat $L_v = 2.5 \times 10^6 \text{ J/kg}$, bulk transfer coefficient for fair weather $C_E = 1.2 \times$
 731 10^{-3} from Large and Pond (1981)⁵⁵, mean wind speed in the tropical eastern Pacific $U_{\text{eq}} = 8 \text{ m/s}$.

732 From the Clausius-Clapeyron relation:

$$\frac{1}{q_s} \frac{dq_s}{dT} = 0.060/\text{K} \implies \frac{dq_s}{dT} = 1.32 \times 10^{-3}/\text{K} \quad (45)$$

733 using 27°C value (December climatology in the tropical eastern Pacific). Since the tropical east-
 734 ern Pacific (180°W – 90°W , 15°S – 15°N) occupies approximately one-quarter of the tropical area,
 735 this local latent heating is distributed over four times the area when considering the total tropical
 736 heating dJ/dT . Therefore, we obtain:

$$\frac{dJ}{dT} \sim \frac{1}{4} \frac{dJ_{\text{local}}}{dT} = \frac{\rho_s L_v C_E U_{\text{eq}}}{4m} \frac{dq_s}{dT} \quad (46)$$

737 Finally, substituting equation (46) into equation (43), circulation intensification per 1 K tropical
 738 eastern Pacific warming is:

$$\frac{dU_0}{dT} \sim \frac{R_d \rho_s L_v C_E U_{\text{eq}}}{8 C_v f U_0 m} \frac{dq_s}{dT} \simeq 0.39 \text{ (m/s)}/\text{K} \quad (47)$$

739 using $m = 1.03 \times 10^4 \text{ kg/m}^2$, $R_d = 287 \text{ J}/(\text{kg} \cdot \text{K})$, $C_v = 717 \text{ J}/(\text{kg} \cdot \text{K})$, $f = 2\Omega \sin(19.0^\circ) =$
 740 $4.7 \times 10^{-5}/\text{s}$.

741 We use the T/M theory's analytical solution $\phi_{\text{TM}}(U_0)$ to convert circulation intensification to
 742 boundary latitude change. Based on equation (47), when 1 K SST change produces typical wind
 743 speed $U_0 + \Delta U_0 = 10.39 \text{ m/s}$, equation (24) gives $\phi_{\text{TM}}(U_0 + \Delta U_0) = 18.1^\circ$. Thus, ENSO-induced
 744 T/M boundary latitude variation is:

$$\frac{d\phi_{\text{TM}}(U_0)}{dT} \simeq \frac{\phi_{\text{TM}}(U_0 + \Delta U_0) - \phi_{\text{TM}}(U_0)}{\Delta T} = \frac{18.1^\circ - 19.0^\circ}{1 \text{ K}} = -0.9^\circ/\text{K} \quad (48)$$

745 Accounting for atmospheric low-pass filter effects obtained in the seasonal variability analysis
746 (phase lag is one month, and amplitude reduces to 65-85% for climate sensitivity $1.5-4.5 \text{ K}/(2 \times$
747 $\text{CO}_2)$):

$$\left(\frac{d\phi_{\text{TM}}(U_0)}{dT}\right)_{\text{low-pass}} = (-0.7^\circ \pm 0.1^\circ)/\text{K} \quad (49)$$

748 which predicts that the T/M boundary latitude shifts equatorward by 0.7° per 1 K tropical eastern
749 Pacific warming.

750 **Data availability**

751 The ERA5 reanalysis data used in this study is available at [https://cds.climate.copernicus.eu/datasets/reanalysis-era5-pressure-levels-monthly-means?tab=](https://cds.climate.copernicus.eu/datasets/reanalysis-era5-pressure-levels-monthly-means?tab=download)
752 [download](https://cds.climate.copernicus.eu/datasets/reanalysis-era5-pressure-levels-monthly-means?tab=download). The NOAA OISST high resolution data set used in Fig. 4 is available at
753 <https://www.esrl.noaa.gov/psd/data/gridded/data.noaa.oisst.v2.highres.html>.
754

755 **Code availability**

756 This study is theoretical in nature and does not involve large-scale numerical simulations. Sim-
757 ple scripts are used for illustrative calculations and figure generation. No specialized code is re-
758 quired to reproduce the main results, which can be obtained directly from the equations presented
759 in the paper.

760 **Acknowledgments**

761 During the preparation of this article, the authors have used Claude 3 and ChatGPT 5.2 for
762 AI-assisted copy editing. After using this service, the authors reviewed and edited the content as
763 needed, and the authors take full responsibility for the content of the publication. The first author
764 is supported by Japan Society for the Promotion of Science (JSPS) KAKENHI Grant Numbers

765 JP23H01241 and JP23K13169, and by the Ministry of Education, Culture, Sports, Science and
766 Technology (MEXT) program for the advanced studies of climate change projection (SENTAN)
767 Grant Number JPMXD0722680395. The second author is supported by JSPS Kakenhi Grant
768 Number JP23K25939. This project is also supported by the Sumitomo Foundation as one of
769 their Environmental Research Projects, and by the Joint Research Program of the Institute of Low
770 Temperature Science, Hokkaido University (25S002).

771 **Author contributions**

772 T.K. led the project, performed all analyses, and wrote the manuscript. H.M. conceived the
773 idea to solve the tropical-midlatitude connection as a boundary layer problem. K.Y. developed
774 the visualization of the virtual lighting in Fig. 2 and improved the mathematical formulation. All
775 authors reviewed and edited the manuscript.

776 **Competing interests**

777 The authors declare no competing interests.

778 **Additional information**

779 **Supplementary Information** is available for this paper.

780 **Correspondence and requests for materials** should be addressed to Tsubasa Kohyama (tsub-
781 asa@is.ocha.ac.jp).

782 **Peer review information** (This part will be completed by Nature staff during proofing.)

783 **Reprints and permissions information** is available at www.nature.com/reprints.

1
2
3
4
5
6
7
8
9
10
11
12
13
14
15
16
17
18

Supplementary information for

“First-principles theory for Earth’s tropical-midlatitude climate boundary”

Tsubasa Kohyama*, Hiroaki Miura, and Kazuya Yamazaki

Department of Information Sciences, Ochanomizu University, Tokyo, Japan

Department of Earth and Planetary Science, The University of Tokyo, Tokyo, Japan

Information Technology Center, The University of Tokyo, Tokyo, Japan

Correspondence and requests for materials should be addressed to Tsubasa Kohyama (tsubasa@is.ocha.ac.jp)

Contents

- Supplementary Text 1. Enthalpy revisited
- Supplementary Text 2. Dynamical “phase transition” across the \mathcal{I}/\mathcal{M} boundary
- Supplementary Figures 1-5

Supplementary Text 1. Enthalpy revisited

Definition

The T/M theory is grounded in thermodynamics expressed through specific enthalpy per unit mass of an ideal gas air parcel:

$$h := c_v T + p\alpha \quad (1)$$

where c_v is specific heat at constant volume, T is temperature, p is pressure, and α is specific volume. The first term on the right-hand side, $c_v T$, is the internal energy per unit mass of the air parcel. The second term, $p\alpha$, is the “pressure-volume energy” possessed by the “mechanical process”, i.e., the dynamical mechanism external to the air parcel that maintains the space occupied by the air parcel. This “pressure-volume energy” is the energy required to maintain a volume α for a gas with pressure p , and it is stored in the mechanical process, not in the air parcel.

To clarify the physical entity of enthalpy, consider the simple system shown in Supplementary Fig. 1a. In this system, a container with gas (mass m , pressure p , temperature T , volume $V = Sh$) is enclosed by a smooth piston of mass M at height h above the bottom in a perfect vacuum with a gravitational field g . We assume that the weight of the piston Mg and the pressure force exerted by the gas on the piston pS are always in balance, maintaining an equilibrium state. In other words, the piston can move quasi-statically while maintaining constant pressure inside. In this system, the total energy of the system including both the gas and the piston (the sum of the internal energy of the gas $mc_v T$ and the gravitational potential energy of the piston $Mgh = pV$) is equal to the enthalpy $mh = mc_v T + pV$.

Most importantly, while the internal energy $mc_v T$ is stored in the gas, the “pressure-volume energy” pV is stored as the potential energy of the piston in the mechanical process, not in the gas. For example, suppose the gas were instantaneously liquefied and removed from the system

41 over an infinitesimally short time. In this case, while the internal energy of the system immediately
42 becomes zero, the potential energy pV required to maintain the void space in the container remains
43 stored in the mechanical process (the piston) during the brief moment before the piston begins to
44 fall to the bottom of the container.

45 *Enthalpy representation of the first law of thermodynamics*

46 The first law of thermodynamics expressed using enthalpy is:

$$dh = \delta q + \alpha dp \quad (2)$$

47 (where δq is the diabatic heating). Here, using the equation of state for an ideal gas and Mayer's
48 relation:

$$dh = c_v dT + d(p\alpha) = c_v dT + R dT = (c_v + R) dT = c_p dT \quad (3)$$

49 (where R is the gas constant and c_p is specific heat at constant pressure), we obtain:

$$\boxed{-\alpha dp = \delta q - c_p dT} \quad (4)$$

50 which is the theoretical foundation of this study.

51 The first law of thermodynamics mandates that any expansion or compression of an air parcel
52 can be expressed as a combination of two distinct processes: an isothermal process that permits
53 heat exchange with its environment, and an adiabatic process that is driven purely by mechanics.
54 These two processes can be illustrated using the piston example (Supplementary Fig. 1b). If
55 the piston is lightened by an amount $-dM$, the gas will expand and depressurize. The first law of
56 thermodynamics requires that the physical process realizing this gas expansion can be decomposed
57 into a combination of two different types of processes. One process is isothermal expansion: the
58 gas is allowed to expand while covered by a heat bath (maintaining $dT = 0$), allowing heat inflow

59 ($\delta q > 0$). The other process is adiabatic expansion: the gas is allowed to expand while covered by
60 a thermal insulator (maintaining $\delta q = 0$), allowing temperature to decrease ($dT < 0$).

61 Equation (4) reveals that, to realize air parcel expansion (depressurization), two distinct enthalpy
62 sources exist that are clearly scale-separated: the “thermal source” (δq), a molecular-scale process,
63 and the “mechanical source” ($-c_p dT$), a macro-scale process at which temperature is definable as
64 a statistical property of the molecular ensemble. Expansion of an air parcel is isothermal-like if
65 the thermal source is dominant, and adiabatic-like if the mechanical source is dominant.

66 Based on local thermodynamic conditions within the air parcel, the thermal source j realizes
67 isothermal expansion (compression) through heating (cooling) from molecular-scale processes.
68 For purely thermal isothermal expansion or compression to occur, temperature adjustment with the
69 surroundings must be sufficiently fast compared to the pressure adjustment timescale. Examples in
70 the climate system include heating from solar radiation, sensible and latent heating, and radiative
71 cooling. In these cases, the air parcel achieves temperature adjustment with the surroundings
72 through gravity wave dissipation. Particularly in the tropics, gravity waves are not interfered with
73 by Earth’s rotation effects, so temperature adjustment with surroundings is carried out efficiently.

74 Based on large-scale dynamic conditions outside the air parcel, the mechanical source $-c_p dT$
75 realizes adiabatic expansion (compression) through changes in a statistical property defined at the
76 molecular ensemble scale. For purely mechanical adiabatic expansion or compression to occur,
77 temperature adjustment with the surroundings must be sufficiently slow compared to the pressure
78 adjustment timescale. Examples in the climate system include external pressure changes induced
79 by cold and warm air advection in the surroundings. Here, again, the air parcel achieves tem-
80 perature adjustment with the surroundings through gravity wave dissipation. Particularly in the
81 midlatitudes, gravity waves possess dispersive properties due to Earth’s rotation effects, so they

82 cannot efficiently transport energy beyond the Rossby deformation radius, and temperature adjust-
83 ment with the surroundings tends to be slow.

84 In atmospheric dynamics, assuming that such adjustment occurs quasi-statically while main-
85 taining local thermodynamic equilibrium, the first law of thermodynamics is employed as a time-
86 evolution equation in the form:

$$\boxed{-\alpha\omega = j - c_p \frac{DT}{Dt}} \quad (5)$$

87 Here, $\omega := Dp/Dt$ is the pressure tendency, j is the diabatic heating rate, and DT/Dt is the
88 temperature tendency. The two terms on the right-hand side of this equation represent the thermal
89 source and mechanical source realizing pressure changes, which are equivalent to vertical motion
90 under hydrostatic balance. Strictly speaking, since these are quantities per unit time, they should
91 be called “the increasing rate” of the thermal and mechanical sources, but in this study, we refer
92 to them simply as thermal source and mechanical source as long as it does not cause confusion.

93 Importantly, the “contribution ratio” of thermal and mechanical sources that realizes pressure
94 changes (i.e., vertical motions) is not determined by the properties of the air parcel itself, but rather
95 by the intrinsic properties of the mechanical process. For example, in the aforementioned piston
96 analogy, if the piston is surrounded by a heat bath, the thermal source realizes the pressure change,
97 whereas if it is surrounded by thermal insulation, the mechanical source realizes the pressure
98 change; the state of the gas itself is irrelevant. Conversely, by manipulating the effective thermal
99 conductivity of the heat bath or insulation, one can choose which enthalpy source supplies the
100 pressure change.

101 Since the mechanical process in the atmosphere varies regionally, regional variations also
102 emerge in which enthalpy source (thermal or mechanical) more readily supplies the energy needed
103 for pressure changes. Specifically, the rate of heat exchange and temperature adjustment with the
104 surroundings is largely constrained by the geographical distributions of fundamental parameters,

105 such as radiation and rotation. Then, the regional characteristics of the “contribution ratio” of
 106 thermal and mechanical sources in realizing pressure changes generates geographic diversity in
 107 atmospheric circulation structure and response characteristics.

108 In particular, under hydrostatic and quasi-geostrophic balance, the thermal source tends primar-
 109 ily to drive the atmosphere in the vertical direction with adjustment occurring through horizontal
 110 motion, whereas the mechanical source tends primarily to drive the atmosphere in the horizontal
 111 direction with adjustment occurring through vertical motion. Indeed, in the thermally-driven case,
 112 buoyancy imposes very localized vertical acceleration, and the magnitude of horizontal divergence
 113 is adjusted to satisfy the continuity equation (Sobel et al. 2001). Conversely, in the mechanically-
 114 driven case, large-scale potential vorticity conservation drives horizontal flow, and vertical motion
 115 is adjusted to satisfy the continuity equation (Supplementary Text 2).

116 *The T/M ratio*

117 In the main text, based on the first law of thermodynamics shown in equation (5), we define
 118 the Thermal-Mechanical ratio. This dimensionless number represents the relative importance of
 119 thermal and mechanical sources for driving vertical motion:

$$\mathcal{T}/\mathcal{M} := \left| \frac{[j]}{[-c_p DT/Dt]} \right| \simeq \left| \frac{[j]}{gDZ_T/Dt} \right| \sim \frac{J}{fU^2} \cdot \frac{L^2}{L_R^2} \quad (6)$$

120 (*see also* Methods). \mathcal{T}/\mathcal{M} is defined at each location and time.

121 \mathcal{T}/\mathcal{M} is different from the reciprocal of the efficiency of a local heat engine, $1/\mathcal{E}$, where
 122 $\mathcal{E} := p(D\alpha/Dt)/j_H$. First of all, \mathcal{T} is defined as the “net” heat source $j = j_H - j_L$ (the differ-
 123 ence between the heating source j_H and cooling source j_L), not solely the heating source j_H as
 124 would appear in the denominator of \mathcal{E} . In addition, \mathcal{M} is defined using the mechanical source
 125 $-c_p DT/Dt$, not the work done by the gas $pD\alpha/Dt$ as would appear in the numerator of \mathcal{E} .

126 *Note on the relationship with dry static energy*

127 In atmospheric dynamics, dry static energy is sometimes used, defined as enthalpy plus the
128 gravitational potential energy of the air parcel:

$$s := h + gZ = c_v T + p\alpha + gZ = c_v T + RT + gZ = c_p T + gZ \quad (7)$$

129 where g is gravitational acceleration and Z is geopotential height. This gZ is the gravitational po-
130 tential energy of the air parcel itself, not the pressure-volume energy $p\alpha$ stored in the mechanical
131 process to maintain the air parcel's space. In the piston example of Supplementary Fig. 1a, this gZ
132 corresponds to the potential energy of the gas when the container is at height Z above the ground.

133 Under the hydrostatic balance approximation, $\alpha\omega \simeq -gDZ/Dt$ holds, so the first law of ther-
134 modynamics can be rewritten using dry static energy as:

$$\frac{Ds}{Dt} \simeq j \quad (8)$$

135 However, the dry static energy representation obscures the role of the mechanical source as an
136 atmospheric driver, so it is not used in this study.

137 **Supplementary Text 2. Dynamical “phase transition” across the \mathcal{T}/\mathcal{M} boundary**

138

139 In this Supplementary Text, to understand the details of the dynamical phase transition that oc-
 140 curs at the T/M boundary, we discuss flows with small Rossby number in a shallow-water system
 141 on a β -plane. The scaling $\mathcal{T}/\mathcal{M} \sim J/(fU^2L_R^2/L^2)$ used in the main text is obtained when as-
 142 suming small Rossby number flow for dynamical variables that are vertically averaged under the
 143 hydrostatic balance assumption. Therefore, it is in complete correspondence with the assumptions
 144 of the equation system used below. Using this correspondence, we show that the WTG system is
 145 derived when $\mathcal{T}/\mathcal{M} \rightarrow \infty$, and the QGPV conservation system is derived when $\mathcal{T}/\mathcal{M} \rightarrow 0$. In
 146 both of these systems, gravity waves are filtered out to extract the essence of large-scale dynamics.

147 *Basic equation*

148 The basic equations considered here are as follows:

$$\begin{cases} \frac{\partial u}{\partial t} + \vec{u} \cdot \vec{\nabla} u - fv = -g \frac{\partial \eta}{\partial x} & (9a) \\ \frac{\partial v}{\partial t} + \vec{u} \cdot \vec{\nabla} v + fu = -g \frac{\partial \eta}{\partial y} & (9b) \\ \frac{\partial \eta}{\partial t} + \vec{u} \cdot \vec{\nabla} \eta + (H + \eta)(\vec{\nabla} \cdot \vec{u}) = \frac{j}{g} & (9c) \end{cases}$$

149 where u is the zonal wind, v is the meridional wind, $\vec{u} := (u, v)$ is the horizontal wind vector, g is
 150 gravitational acceleration, η is height perturbation, H is equivalent depth, j is the net heat source,
 151 and the Coriolis parameter is $f = f_0 + \beta y$.

152 Using Rossby number $\text{Ro} := U/f_0L$ and Burger number $\text{Bu} := (L_R/L)^2 = gH/f_0^2L^2$, and typical
 153 heating scale $J \sim \text{Ro} \mathcal{J}$, we nondimensionalize the variables by defining the scale of each variable

154 as follows¹:

$$(u, v) = U(\hat{u}, \hat{v}) \quad (10)$$

$$(x, y) = L(\hat{x}, \hat{y}) \quad (11)$$

$$\eta = \text{BuRo}H\hat{\eta} = \frac{f_0UL}{g}\hat{\eta} \quad (12)$$

$$\beta = \text{Ro}\frac{f_0}{L}\hat{\beta} \quad (13)$$

$$j = J\hat{j} = \text{Ro}\mathcal{J}\hat{j} \quad (14)$$

155 These scalings are chosen so that geostrophic balance holds when the Rossby number is suffi-
 156 ciently small ($\text{Ro} \ll 1$), with $f_0U \sim g\{\eta\}/L$ and the effects of β and j being negligible.

157 The scaling of time t is not straightforward, because the timescales of the momentum equa-
 158 tions and the continuity equation are not necessarily equal. First, the timescale in the momentum
 159 equations is determined by the advective timescale L/U , so we nondimensionalize it as:

$$t = \frac{L}{U}\hat{t} \quad (15)$$

160 Then, the timescale in the continuity equation is determined roughly by the response timescale of
 161 the height field (pressure field) to divergence and convergence. Although this timescale has not
 162 yet been determined, for convenience of exposition, we use the divergence scale $\text{Ro}U/L$ derived
 163 later and write:

$$\left\{ \frac{D\eta}{Dt} \right\} \sim \left\{ H \left(\frac{\partial u}{\partial x} + \frac{\partial v}{\partial y} \right) \right\} \implies \frac{\{\eta\}}{T} \sim H\text{Ro}\frac{U}{L} \quad (16)$$

164 This scaling is justified by the fact that the resulting equations do not become inconsistent. Sub-
 165 stituting equation (12) into this relation determines the timescale of the continuity equation as

¹The Burger number used here has a reciprocal relationship with the definition given by Sobel et al. (2001), $\text{Bu} := (L/L_R)^2$, but here we follow the convention in fluid dynamics.

166 $T \sim (L/U)/\text{Bu}$. That is, the time t in the continuity equation is nondimensionalized as:

$$t = \frac{L}{U\text{Bu}}\hat{t} \quad (17)$$

167 Using these scalings, the nondimensional equations are:

$$\left\{ \begin{array}{l} \text{Ro} \left(\frac{\partial \hat{u}}{\partial \hat{t}} + \hat{u} \cdot \hat{\nabla} \hat{u} \right) - (1 + \text{Ro}\hat{\beta}\hat{y})\hat{v} = -\frac{\partial \hat{\eta}}{\partial \hat{x}} \end{array} \right. \quad (18a)$$

$$\left\{ \begin{array}{l} \text{Ro} \left(\frac{\partial \hat{v}}{\partial \hat{t}} + \hat{u} \cdot \hat{\nabla} \hat{v} \right) + (1 + \text{Ro}\hat{\beta}\hat{y})\hat{u} = -\frac{\partial \hat{\eta}}{\partial \hat{y}} \end{array} \right. \quad (18b)$$

$$\left\{ \begin{array}{l} \text{Ro} \left(\frac{\partial \hat{\eta}}{\partial \hat{t}} + \hat{u} \cdot \hat{\nabla} \hat{\eta} + \frac{\hat{\eta}}{\text{Bu}} \hat{\nabla} \cdot \hat{u} \right) + \hat{\nabla} \cdot \hat{u} = \text{Da}\hat{j} \end{array} \right. \quad (18c)$$

168 Here, the Damköhler number is defined as:

$$\text{Da} := \frac{JL}{gHU} = \text{Ro} \frac{\mathcal{J}L}{gHU} \quad (19)$$

169 The Damköhler number is a nondimensional number conventionally used in chemical engineering
 170 to represent the ratio of the reaction rate to the transport rate. Here, it represents the ratio of the
 171 heating response (J/gH) to the advection (U/L).²

172 *Rossby number expansion*

173 Considering large-scale dynamics with $\text{Ro} \ll 1$, we perform a Rossby number expansion of the
 174 basic equations:

$$\left\{ \begin{array}{l} \hat{u} = \hat{u}_0 + \text{Ro}\hat{u}_1 + \text{Ro}^2\hat{u}_2 + \dots \end{array} \right. \quad (20a)$$

$$\left\{ \begin{array}{l} \hat{v} = \hat{v}_0 + \text{Ro}\hat{v}_1 + \text{Ro}^2\hat{v}_2 + \dots \end{array} \right. \quad (20b)$$

$$\left\{ \begin{array}{l} \hat{\eta} = \hat{\eta}_0 + \text{Ro}\hat{\eta}_1 + \text{Ro}^2\hat{\eta}_2 + \dots \end{array} \right. \quad (20c)$$

$$\left\{ \begin{array}{l} \hat{j} = \hat{j}_0 + \text{Ro}\hat{j}_1 + \text{Ro}^2\hat{j}_2 + \dots \end{array} \right. \quad (20d)$$

²In other words, it is the ratio of “advective transport time (L/U)” to “adjustment time of the field to divergence/convergence by heating ($gH/\{j\}$)”. For example, the larger the heating, the more energy is injected into the system per unit time, the shorter the time required to change the dynamical field, and the smaller the role of advection.

175 Substituting these into equations (18a)-(18c), the equations of $O(1)$ are:

$$\left\{ \begin{array}{l} -v_0 = -\frac{\partial \hat{\eta}_0}{\partial \hat{x}} \end{array} \right. \quad (21a)$$

$$\left\{ \begin{array}{l} u_0 = -\frac{\partial \hat{\eta}_0}{\partial \hat{y}} \end{array} \right. \quad (21b)$$

$$\left\{ \begin{array}{l} \vec{\nabla} \cdot \vec{u}_0 = 0 \end{array} \right. \quad (21c)$$

176 and those of $O(\text{Ro})$ are:

$$\left\{ \begin{array}{l} \frac{\partial \hat{u}_0}{\partial \hat{t}} + \hat{u}_0 \cdot \hat{\nabla} \hat{u}_0 - \hat{v}_1 - \hat{\beta} \hat{y} \hat{v}_0 = -\frac{\partial \hat{\eta}_1}{\partial \hat{x}} \end{array} \right. \quad (22a)$$

$$\left\{ \begin{array}{l} \frac{\partial \hat{v}_0}{\partial \hat{t}} + \hat{u}_0 \cdot \hat{\nabla} \hat{v}_0 + \hat{u}_1 + \hat{\beta} \hat{y} \hat{v}_0 = -\frac{\partial \hat{\eta}_1}{\partial \hat{y}} \end{array} \right. \quad (22b)$$

$$\left\{ \begin{array}{l} \frac{\partial \hat{\eta}_0}{\partial \hat{t}} + \hat{u}_0 \cdot \hat{\nabla} \hat{\eta}_0 + \frac{\hat{\eta}_0}{\text{Bu}} \hat{\nabla} \cdot \hat{u}_0 + \hat{\nabla} \cdot \hat{u}_1 = \frac{JL}{gHU} \hat{j}_0 \end{array} \right. \quad (22c)$$

177 Rewriting these equations in terms of divergence and vorticity, which are defined as:

$$\hat{\delta}_0 := \frac{\partial \hat{u}_0}{\partial \hat{x}} + \frac{\partial \hat{v}_0}{\partial \hat{y}}, \quad \hat{\delta}_1 := \frac{\partial \hat{u}_1}{\partial \hat{x}} + \frac{\partial \hat{v}_1}{\partial \hat{y}}, \quad \dots \quad (23)$$

$$\hat{\zeta}_0 := \frac{\partial \hat{v}_0}{\partial \hat{x}} - \frac{\partial \hat{u}_0}{\partial \hat{y}}, \quad \hat{\zeta}_1 := \frac{\partial \hat{v}_1}{\partial \hat{x}} - \frac{\partial \hat{u}_1}{\partial \hat{y}}, \quad \dots \quad (24)$$

179 and denoting the Lagrangian derivative along geostrophic winds as $D_0/D\hat{t}$, we obtain a set of
180 equations³ for $\hat{\zeta}_0$, $\hat{\delta}_1$, and $\hat{\eta}_0$:

$$\left\{ \begin{array}{l} \frac{D_0 \hat{\zeta}_0}{D\hat{t}} + \hat{\delta}_1 + \hat{\beta} \frac{\partial \hat{\eta}_0}{\partial \hat{x}} = 0 \end{array} \right. \quad (27a)$$

$$\left\{ \begin{array}{l} \frac{D_0 \hat{\eta}_0}{D\hat{t}} + \hat{\delta}_1 = \frac{\text{Da}}{\text{Ro}} \hat{j}_0 \end{array} \right. \quad (27b)$$

$$\left\{ \begin{array}{l} \hat{\zeta}_0 = \hat{\nabla}^2 \hat{\eta}_0 \end{array} \right. \quad (27c)$$

³Taking the derivative of equation (22b) with respect to \hat{x} and subtracting the derivative of equation (22a) with respect to \hat{y} , we obtain:

$$\frac{\partial}{\partial \hat{x}} \left(\frac{\partial \hat{v}_0}{\partial \hat{t}} \right) - \frac{\partial}{\partial \hat{y}} \left(\frac{\partial \hat{u}_0}{\partial \hat{t}} \right) + \frac{\partial}{\partial \hat{x}} (\hat{u}_0 \cdot \hat{\nabla} \hat{v}_0) - \frac{\partial}{\partial \hat{y}} (\hat{u}_0 \cdot \hat{\nabla} \hat{u}_0) + \frac{\partial \hat{u}_1}{\partial \hat{x}} + \hat{\beta} \hat{y} \frac{\partial \hat{u}_0}{\partial \hat{x}} + \frac{\partial \hat{v}_1}{\partial \hat{y}} + \hat{\beta} \hat{y} \frac{\partial \hat{v}_0}{\partial \hat{y}} + \hat{\beta} \hat{v}_0 = 0 \quad (25)$$

The nonlinear terms $\frac{\partial}{\partial \hat{x}} (\hat{u}_0 \cdot \hat{\nabla} \hat{v}_0) - \frac{\partial}{\partial \hat{y}} (\hat{u}_0 \cdot \hat{\nabla} \hat{u}_0)$ can be rewritten using vector identities as $\hat{u}_0 \cdot \hat{\nabla} \hat{\zeta}_0 + \hat{\delta}_0 \hat{\zeta}_0$, giving:

$$\frac{\partial \hat{\zeta}_0}{\partial \hat{t}} + \hat{u}_0 \cdot \hat{\nabla} \hat{\zeta}_0 + \hat{\delta}_0 \hat{\zeta}_0 + \hat{\delta}_1 + \hat{\beta} \hat{y} \hat{\delta}_0 + \hat{\beta} \hat{v}_0 = 0 \quad (26)$$

Substituting $\hat{\delta}_0 = 0$ into equation (26) and equation (22c), we obtain equations (27a) and (27b), respectively. Furthermore, from equations (21a) and (21b), we obtain equation (27c).

181 Note that, from equation (21c), we have $\hat{\delta}_0 = 0$. Since the solution of the quasi-geostrophic system
 182 generally has $\hat{\delta}_1 \neq 0$, the divergence scales as $\{\delta\} \sim \text{Ro}U/L$.

183 If we neglect quantities higher than the leading order in Rossby number according to:

$$\hat{\zeta} \simeq \hat{\zeta}_0, \quad \hat{\eta} \simeq \hat{\eta}_0, \quad \hat{\delta} \simeq \text{Ro}\hat{\delta}_1, \quad \frac{D}{D\hat{t}} \simeq \frac{D_0}{D\hat{t}}, \quad \hat{j} \simeq \hat{j}_0 \quad (28)$$

184 we obtain:

$$\left\{ \begin{array}{l} \text{Ro} \frac{D\hat{\zeta}}{D\hat{t}} + \hat{\delta} + \text{Ro}\hat{\beta} \frac{\partial \hat{\eta}}{\partial \hat{x}} = 0 \\ \hat{\delta} = -\text{Ro} \frac{D\hat{\eta}}{D\hat{t}} + \text{Da}\hat{j} \\ \hat{\zeta} = \hat{\nabla}^2 \hat{\eta} \end{array} \right. \quad (29a)$$

$$\hat{\delta} = -\text{Ro} \frac{D\hat{\eta}}{D\hat{t}} + \text{Da}\hat{j} \quad (29b)$$

$$\hat{\zeta} = \hat{\nabla}^2 \hat{\eta} \quad (29c)$$

185 or dimensionally,

$$\left\{ \begin{array}{l} \frac{D\zeta}{Dt} + \delta + \frac{\beta g}{f_0} \frac{\partial \eta}{\partial x} = 0 \end{array} \right. \quad (30a)$$

$$\left\{ \begin{array}{l} \delta = -\frac{1}{H} \frac{D\eta}{Dt} + \frac{j}{gH} \end{array} \right. \quad (30b)$$

$$\left\{ \begin{array}{l} \zeta = \frac{g}{f_0} \nabla^2 \eta \end{array} \right. \quad (30c)$$

186 This is the quasi-geostrophic system with diabatic heating.

187 *Derivation of the WTG and QGPV conservation systems based on \mathcal{T}/\mathcal{M}*

188 Combining the nondimensional parameters appearing in equation (29b):

$$\frac{\text{Da}}{\text{Ro}} = \frac{JL/gHU}{U/fL} = \frac{J}{fU^2} \cdot \frac{f^2 L^2}{gH} = \frac{J}{fU^2} \cdot \frac{L^2}{L_R^2} \sim \mathcal{T}/\mathcal{M} \quad (31)$$

189 Therefore, in this shallow-water system:

$$\left\{ \begin{array}{l} \mathcal{T}/\mathcal{M} \rightarrow \infty \iff \text{Da} \gg \text{Ro} \\ \mathcal{T}/\mathcal{M} \rightarrow 0 \iff \text{Da} \ll \text{Ro} \end{array} \right. \quad (32a)$$

$$\left\{ \begin{array}{l} \mathcal{T}/\mathcal{M} \rightarrow 0 \iff \text{Da} \ll \text{Ro} \end{array} \right. \quad (32b)$$

190 When $\mathcal{T}/\mathcal{M} \rightarrow \infty$ (with $\text{Da} \gg \text{Ro}$), setting $\text{Da} \gg \text{Ro}$ in equation (29b), we obtain the following
 191 WTG system:

$$\left\{ \begin{array}{l} \frac{D\zeta}{Dt} + \frac{\beta g}{f_0} \frac{\partial \eta}{\partial x} = -\frac{f_0}{gH} j \end{array} \right. \quad (33a)$$

$$\left\{ \begin{array}{l} \delta = \frac{j}{gH} \end{array} \right. \quad (33b)$$

$$\left\{ \begin{array}{l} \zeta = \frac{g}{f_0} \nabla^2 \eta \end{array} \right. \quad (33c)$$

192 Here, the first equation represents “conservation of absolute vorticity,” the second equation rep-
 193 resents “balance between divergence and heating,” and the third equation represents “geostrophic
 194 balance.” Geostrophic balance holds widely in the WTG system except very close to the equa-
 195 tor where the Rossby number becomes large (Supplementary Fig. 2). As is evident from these
 196 equations, in the WTG system, there is no distinction between potential vorticity and absolute
 197 vorticity.

198 Next, when $\mathcal{T}/\mathcal{M} \rightarrow 0$ (with $\text{Da} \ll \text{Ro}$), setting $\text{Da} \ll \text{Ro}$ in equation (29b), we obtain the
 199 following QGPV conservation system:

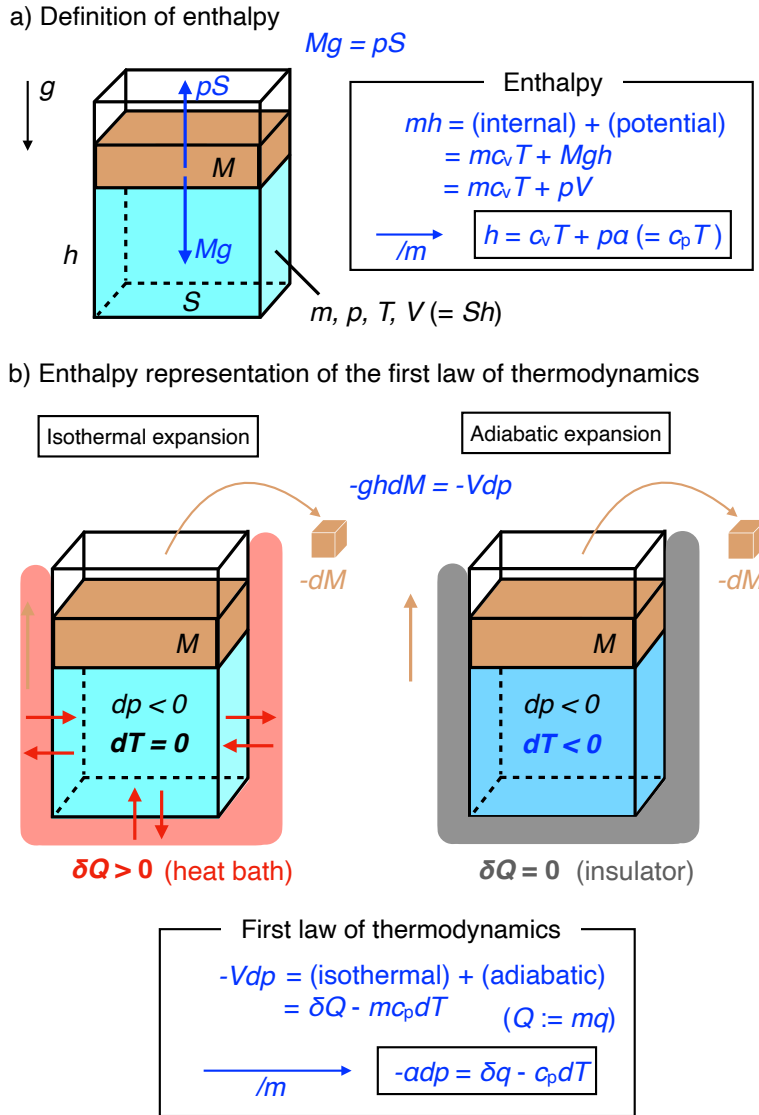
$$\left\{ \begin{array}{l} \frac{D\zeta}{Dt} + \frac{\beta g}{f_0} \frac{\partial \eta}{\partial x} - \frac{f_0}{H} \frac{D\eta}{Dt} = 0 \end{array} \right. \quad (34a)$$

$$\left\{ \begin{array}{l} \delta = -\frac{1}{H} \frac{D\eta}{Dt} \end{array} \right. \quad (34b)$$

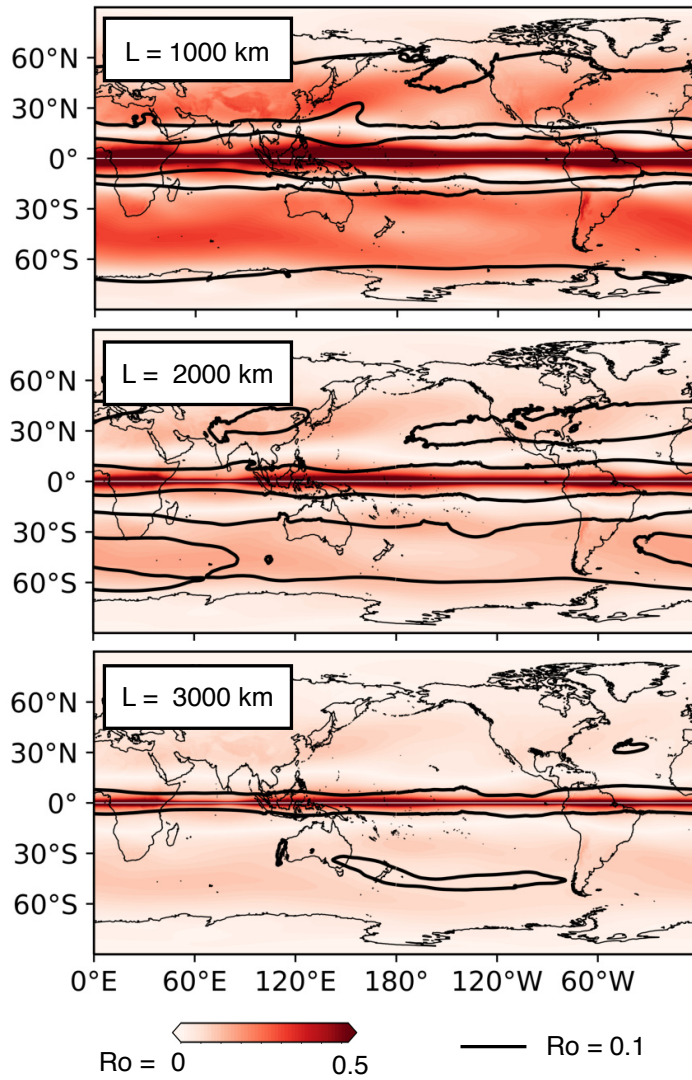
$$\left\{ \begin{array}{l} \zeta = \frac{g}{f_0} \nabla^2 \eta \end{array} \right. \quad (34c)$$

200 Here, the first equation represents “quasi-geostrophic potential vorticity conservation,” the second
 201 equation represents “continuity equation,” and the third equation represents “geostrophic balance.”
 202 In the QGPV conservation system, the mechanical source dominates over the thermal source as
 203 a driving force, so the QGPV defined on the left-hand side of the first equation is conserved.
 204 Divergence (i.e., vertical motion) is then determined diagnostically from the continuity equation
 205 (second equation) in a way that satisfies QGPV conservation.

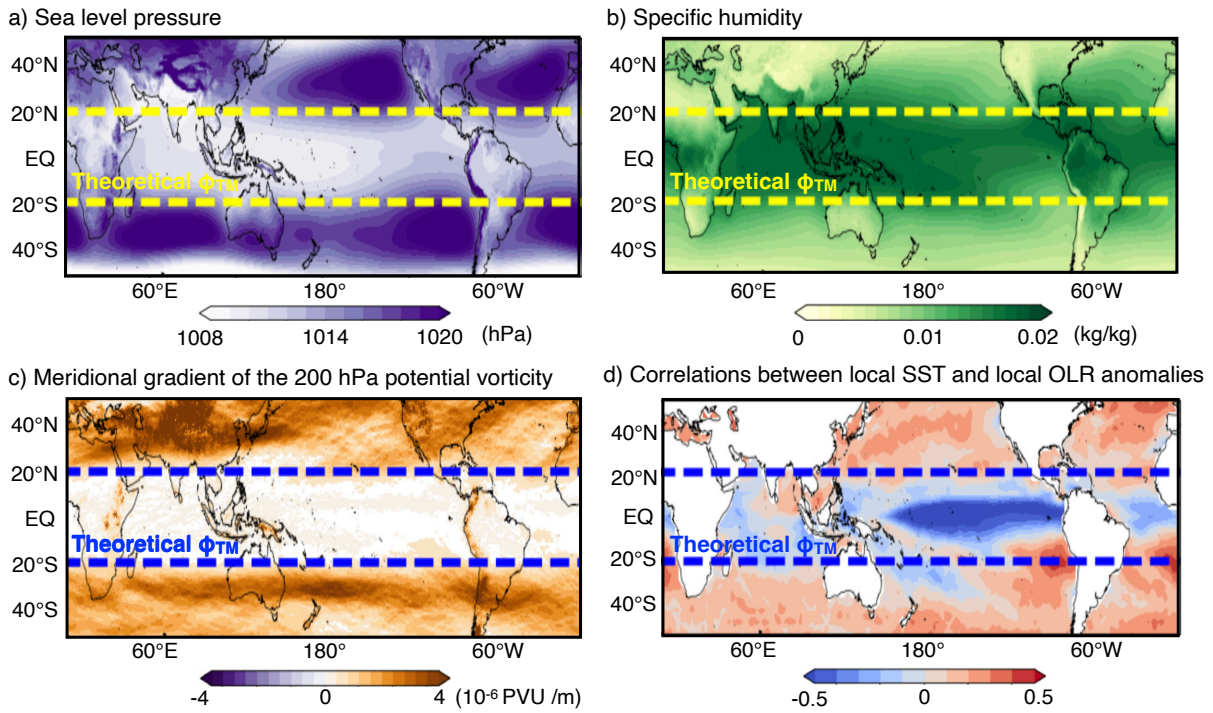
206 From these results, it is shown that \mathcal{I}/\mathcal{M} is the parameter determining the “phase transition”
207 between the WTG system and the QGPV conservation system, which are known to dominate in
208 the tropics and in the midlatitudes, respectively. Combined with the results of the previous section,
209 it is shown that two interior regions with different reasons for existence, i.e., the WTG atmosphere
210 ($\mathcal{I}/\mathcal{M} \rightarrow \infty$) and the QGPV conservation atmosphere ($\mathcal{I}/\mathcal{M} \rightarrow 0$), are smoothly connected at
211 a “boundary layer” where $\mathcal{I}/\mathcal{M} \sim 10$, that is, near latitude $\phi_{TM} \simeq 19^\circ$.



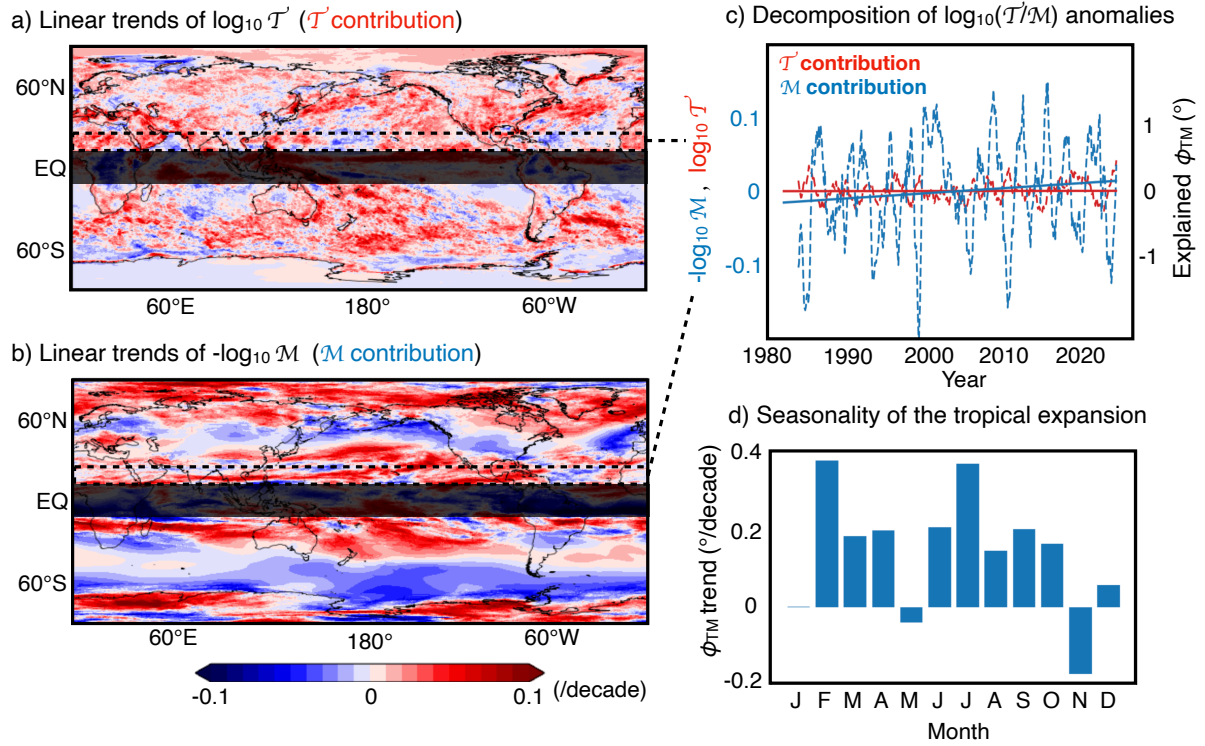
213 **FIG. 1. Enthalpy and its representation of the energy conservation.** (a) Schematic explaining the defini-
 214 tion of enthalpy using a system that consists of a container, a piston, and air. (b) Schematic showing the two
 215 possible processes (i.e., isothermal and adiabatic expansions) to decrease air pressure, explaining the enthalpy
 216 representation of the first law of thermodynamics.



217 **FIG. 2. Spatial distribution of the Rossby number.** Annual-mean Rossby number in 2024 calculated as
 218 U/fL , where U is the mass-weighted vertical-mean wind (*see Methods*), f is Coriolis parameter, and L is the
 219 horizontal scale.

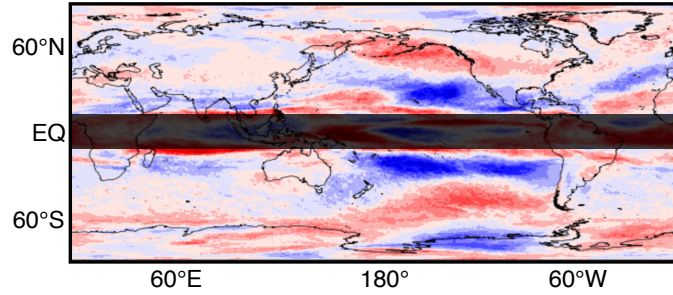


220 FIG. 3. **Implications of the T/M theory for various meteorological variables.** (a) Annual-mean sea level
 221 pressure in 2024. (b) Annual-mean specific humidity at 500 hPa in 2024. (c) Annual-mean meridional potential
 222 vorticity gradient at 200 hPa in 2024. 1 PVU = 10^{-6} (K·m²)/(kg·s). (d) Correlation coefficients between local
 223 SST and local outgoing longwave radiation calculated for 1982-2024 at each 2.5-degree global grid.

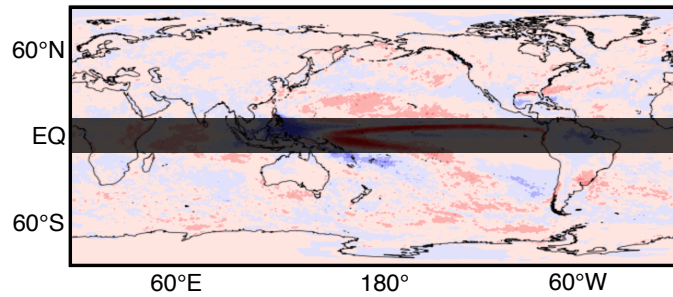


224 FIG. 4. Analysis on the “global tropicalization” and its associated tropical expansion. (a) Top, As in Fig.
 225 4a, but for $\log_{10} \mathcal{T}$. Bottom, As in Fig. 4a, but for $-\log_{10} \mathcal{M}$. (b) As in the blue dashed curve in Fig. 4b,
 226 but for $\log_{10} \mathcal{T}$ (red) and $-\log_{10} \mathcal{M}$ (blue). (d) Seasonal variability of zonal-mean ϕ_{TM} trends in the Northern
 227 Hemisphere.

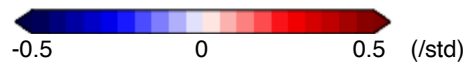
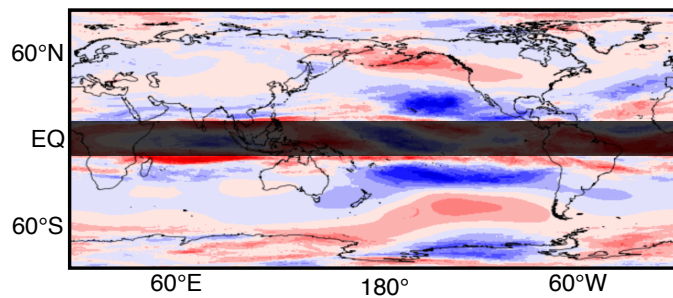
a) Regression map of $\log_{10}(\mathcal{T}/\mathcal{M})$ anomalies on Niño3.4



b) As in (a), but for $\log_{10}(\mathcal{T})$ (\mathcal{T} contribution)



c) As in (a), but for $-\log_{10}(\mathcal{M})$ (\mathcal{M} contribution)



228 FIG. 5. **The T/M response to ENSO.** (a) Regression map of $\log_{10} \mathcal{T} / \mathcal{M}$ onto the Niño 3.4 index (blue curve
 229 in Fig. 4d). (b) As in (a), but for $\log_{10} \mathcal{T}$. (c) As in (a), but for $-\log_{10} \mathcal{M}$.